Computer Methods in Applied Mechanics and Engineering 437 (2025) 117773

Contents lists available at ScienceDirect

Comput. Methods Appl. Mech. Engrg.

journal homepage: www.elsevier.com/locate/cma

Interval Isogeometric Analysis for coping with geometric uncertainty

Nataly A. Manque [a,*], Jan Liedmann [b], Franz-Joseph Barthold [c], Marcos A. Valdebenito [a], Matthias G.R. Faes [a,d]

[a] Chair for Reliability Engineering, TU Dortmund University, Leonhard-Euler-Str. 5, Dortmund 44227, Germany
[b] Institute of Structural Mechanics and Dynamics in Aerospace Engineering, University of Stuttgart, Pfaffenwaldring 27, 70569 Stuttgart, Germany
[c] Institut für Baumechanik, Statik und Dynamik, Technische Universität Dortmund, August-Schmidt-Str. 8, 44227 Dortmund, Germany
[d] International Joint Research Center for Engineering Reliability and Stochastic Mechanics, Tongji University, Shanghai 200092, China

ARTICLE INFO

Keywords:
Isogeometric analysis (IGA)
Geometric uncertainty
Interval analysis
Variational sensitivity analysis
Stress triaxiality

ABSTRACT

Geometric uncertainty poses a significant challenge in many engineering sub-disciplines ranging from structural design to manufacturing processes, often attributed to the underlying manufacturing technology and operating conditions. When combined with geometric complexity, this phenomenon can result in substantial disparities between numerical predictions and the actual behavior of mechanical systems. One of the underlying causes lies in the initial design phase, where insufficient information impedes the development of robust numerical models due to epistemic uncertainty in system dimensions. In such cases, set-based methods, like intervals, prove useful for characterizing these uncertainties by employing lower and upper bounds to define uncertain input parameters. Nevertheless, employing interval methods for treating geometric uncertainties can become computationally demanding, especially when traditional methods like finite element analysis (FEA) are utilized to represent the system. This is due to the necessity of performing iterative analyses for different realizations of geometry within the bounds of uncertain parameters, requiring the repeated execution of the meshing process and thereby escalating the numerical effort. Moreover, the process of remeshing introduces a second challenge by disrupting the continuity of the underlying optimization problem inherent in interval analysis, further complicating the computational procedure. In this work, the potential of Isogeometric Analysis (IGA) for quantifying geometric uncertainties characterized by intervals is explored. IGA utilizes the same basis functions, Non-Uniform Rational B-Splines (NURBS), employed in Computer-Aided Design (CAD) to approximate solution fields in numerical analysis. This integration enhances the accurate description of complex shapes and interfaces while maintaining geometric fidelity throughout the simulation process. The primary advantage of employing IGA for uncertainty quantification lies in its ability to control the system's geometry through the position of control points, which define the shape of NURBS. Consequently, alterations in the model's geometry can be achieved by varying the position of these control points, thereby bypassing the numerical costs associated with remeshing when performing uncertainty quantification considering intervals. To propagate geometric uncertainties, a gradient-based optimization (GBO) algorithm is applied to determine the lower and upper bounds of the system response. The corresponding sensitivities are computed from the IGA model with a variational

* Corresponding author.
E-mail address: nataly.manque@tu-dortmund.de (N.A. Manque).

https://doi.org/10.1016/j.cma.2025.117773
Received 14 October 2024; Received in revised form 15 January 2025; Accepted 16 January 2025
Available online 30 January 2025

approach. Two case studies involving linear systems with uncertain geometric parameters demonstrate that the proposed strategy accurately estimates uncertain stress triaxiality.

1. Introduction

Geometric uncertainties are prevalent in fields as diverse as aerospace, automotive, robotics, and civil, mechanical, and biomedical engineering, where precision and robustness are paramount [1]. These uncertainties can pose significant challenges to ensuring the performance and safety of critical systems. In industrial manufacturing, for example, geometric uncertainties play a critical role in the design and production process. For such reason, manufacturing geometric uncertainty will be the focus of this work. Manufacturing geometric uncertainty involves discrepancies between nominal models and the actual behavior of a component, potentially resulting in inaccuracies in dimensions, shape, and tolerances of the manufactured part [2,3]. This phenomenon can contribute to diminished working efficiency, variations in the performance of mechanical systems, as well as decreased service life and operational reliability [4,5]. Various sources can contribute to geometric uncertainties in manufacturing processes. For instance, wear and deflection of cutting tools may lead to deviations from the intended geometry during machining processes [6]. Inaccuracies and imperfections in the machine tool itself, such as backlash, thermal expansion, or misalignment, can also introduce geometric uncertainties [7–9]. Additionally, elastic and plastic deformation of materials during machining or forming processes may induce deviations from the desired geometry [10]. Moreover, inconsistent or imprecise fixtures and clamping mechanisms can introduce variations in part positioning, impacting the final geometry [11]. Since all these causes can affect the final operating conditions of the system, such geometric uncertainties must be taken into account to accurately study the behavior of mechanical components.

The geometry information available during the initial design phase is typically limited and inaccurate due to the aforementioned manufacturing sources of geometric uncertainty. This lack of knowledge impedes the development of robust numerical models due to epistemic uncertainty in system dimensions. In recent years, set-based methods have been developed to address uncertainty arising from information scarcity [12,13]. These methods have been widely applied to estimate system responses resulting from epistemic uncertainty, including fuzzy analysis [14,15], imprecise probabilities [16,17], and interval analysis [18–21]. Among these techniques, interval analysis has proven particularly practical when dealing with limited information [22,23]. In interval analysis, a parameter affected by epistemic uncertainty is defined by lower and upper bounds [24]. This approach is especially suitable at an earlier stage of design when only the range of variation of the uncertain parameters is known, and the available information is insufficient to determine the nature of the distribution within the interval [25]. Once uncertainty is described by intervals, it is necessary to propagate this uncertainty to the response of interest (e.g., displacements, strains, and stresses). Traditionally, interval uncertain parameters are propagated through a finite element model (FE) to obtain information about the extremes of the system response using a global optimization approach [26]. Nevertheless, performing interval analysis can be computationally expensive, especially for complex models with numerous uncertain parameters [27]. The need to repeatedly evaluate the numerical model over different interval realizations increases the computational cost. This cost is even higher when geometric parameters are uncertain, as in the case of manufacturing uncertainties. This is because each of these evaluations requires rebuilding the finite element geometry (i.e., the mesh), which is costly, time-consuming, and increases the inaccuracy of the geometry representation. Moreover, a second problem with remeshing procedures is that it destroys the continuity of the optimization problem underlying interval analysis.

The motivation for this paper is to explore the potential of Isogeometric Analysis (IGA) [28] for quantifying geometric uncertainties characterized by intervals. In this technique, geometries described by Non-Uniform Rational B-Splines (NURBS) based on Computer-Aided Design (CAD) are used directly in the analysis framework, without performing any geometric approximation as in the Finite Element Analysis (FEA) [29]. Therefore, the main principle of IGA is to use NURBS basis functions to construct and manipulate the exact shape of CAD geometries and as a means for their numerical analysis [30]. Notably, NURBS exhibit meaningful properties, including non-negativity, unit partitioning, local support, and smoothness, ensuring high-order continuity between elements [31]. As a result, one of the main advantages of IGA is its geometric accuracy [32], no matter how coarse the discretization may be [28]. Since IGA allows users to easily handle complex geometries, this technique seems suitable for uncertainty quantification (UQ) [31]. To the best of our knowledge, a few applications of IGA for UQ have been developed. The work of [33] uses the Stochastic Isogeometric Analysis (SIGA) to study the free vibration of functionally graded plates with spatially varying random material properties. In their work, the elastic modulus and mass density were considered uncertain properties, which were modeled as homogeneous Gaussian random fields. Spectral stochastic isogeometric analysis (SSIGA) [34] for stochastic linear elasticity problems considering spatially dependent uncertain Young's modulus has also been investigated. The contribution of [35] proposes an IGA-based framework for solving the uncertainty problem of composite shells. The work of [36] presents a framework for uncertainty quantification and robust shape optimization of acoustic structures. The approach is based on the Boundary Element Method (BEM) and the Polynomial Chaos Expansion (PCE), where an IGA BEM is used to calculate shape sensitivities. Another contribution of SIGA to the analysis of shape uncertainty has been proposed by [37], where the authors combine IGA and PCE to address uncertainty described by random fields. Nevertheless, the application of IGA to quantify geometric uncertainties under limited data has not been explored. Hence, it is the object of this work to examine its coupling with interval analysis. When using IGA to model a system, the geometry can be controlled by the position of the control points that define the shape of the NURBS [38]. This is an advantage for quantifying geometric uncertainty. This is because the control points define the control mesh, which represents the physical structure of the system. As a result, it is possible to modify the model geometry and obtain the updated field solutions without going through the remeshing process [39,40]. Therefore, by manipulating the geometry through changes in the position of

the control points, it is possible to avoid the numerical cost of performing interval analysis using classical finite element analysis with remeshing.

For the propagation of geometric uncertainties, applying a gradient-based optimization (GBO) algorithm [41] is proposed to determine both the lower and upper bounds of the system response. The gradient of the objective function is calculated concerning each geometric uncertain parameter, from the sensitivities of the IGA model. Exploiting the key benefit of IGA to manipulate the geometry, a variational formulation that allows the simultaneous computation of structural response and sensitivities is applied [42]. A parameterization of the NURBS control point matrix is applied to guide FE users in the use of IGA for uncertainty quantification. The proposed strategy is tested for estimating uncertain stress triaxiality in a linear 2D hook system with uncertain radius and thickness, and in a linear 3D horseshoe shape with four uncertain geometric parameters.

The rest of the paper is organized as follows. The governing equations for the class of systems considered in this work are presented in Section 2. The definition of the response of interest as well as the influence of geometric uncertainty on the associated stress triaxiality response is also explained. Section 3 presents the approach used to describe the uncertain parameters associated with the geometry using interval analysis. The disadvantages of interval analysis for uncertainty propagation in the context of FEA are discussed in detail. Section 4 provides the basics of IGA analysis and the formulation of the sensitivity analysis. The applied uncertainty propagation scheme is presented in Section 5, using the GBO algorithm. The implementation of the proposed technique is illustrated and discussed in Section 6. Conclusions are drawn in Section 7.

2. Formulation of the problem

2.1. Governing equations

Consider a linear system under the influence of static loads. It is considered that the parameters that characterize the geometry of the system (e.g., lengths, thicknesses, curvatures) cannot be accurately determined due to problems such as lack of knowledge, vagueness, and imprecision of data resulting from manufacturing processes. Consequently, the geometric input parameters are affected by epistemic uncertainty. These parameters are collected in a vector $\boldsymbol{x}$ of dimension n_x. Typically, a set of partial differential equations (PDEs) must be solved to perform a structural design calculation for this system. The approximate solution of these PDEs is usually provided by a numerical model $\mathcal{M}(\boldsymbol{x})$. This numerical model $\mathcal{M}(\boldsymbol{x})$ can be constructed using the Finite Element Method (FEM) [43], Finite Difference Method (FDM) [44], Boundary Element Method (BEM) [45], or Isogeometric Analysis (IGA) [28], among others. Note that the model $\mathcal{M}(\boldsymbol{x})$ depends on the geometric uncertain parameters $\boldsymbol{x}$. In addition, through the application of these methods, the model yields a response $\boldsymbol{y}$, which is defined as,

$$\mathcal{M}(\boldsymbol{x}) : \boldsymbol{y} = m(\boldsymbol{x}) \tag{1}$$

where m is a response function operator that maps the geometric uncertain input parameters $\boldsymbol{x}$ to the output response $\boldsymbol{y}$. This response can encompass various quantities of interest, such as displacements, stresses, or strain fields. Note that the behavior of the system, given by its response $\boldsymbol{y}$, is influenced by uncertain geometric variables $\boldsymbol{x}$ during the mapping with m. As a result, the response of the system is subject to uncertainties as well. The response of interest considered in this paper is discussed in Section 2.2.

Notably, the construction of the numerical model $\mathcal{M}(\boldsymbol{x})$ using the traditional finite element method can involve significant computational effort, especially when the uncertainty relates to geometry. Firstly, a large number of degrees-of-freedom are typically required to discretely represent a system with traditional FEA, to accurately capture its real behavior. This becomes especially challenging when dealing with complex geometries. Secondly, the discretization step involves defining a finite element mesh that approximates the system's real geometry. To capture uncertainties in the geometry, this mesh needs redefinition whenever the geometry changes. As a result, the numerical model $\mathcal{M}(\boldsymbol{x})$ must be constructed at a high level of detail to accurately capture the complex geometry of the system and is further dependent on the mesh definition. Consequently, obtaining a solution for Eq. (1) may not be straightforward in the presence of geometric uncertainty. Therefore, exploring alternative methods becomes essential to reduce computational costs and increase efficiency when analyzing systems with complex geometries and uncertain parameters. Hence, this paper investigates Isogeometric Analysis (IGA) as an alternative method due to its advantages in handling geometry. The basis of this technique will be discussed in Section 4.

2.2. Stress triaxiality

As mentioned above, it is of interest to investigate a response related to the system defined in Eq. (1), e.g. for design purposes. In mechanical analysis and especially in manufacturing design, users are interested in studying damage states [46], as well as initiation of fracture processes [47]. For this purpose, analyzing the stresses resulting from the numerical simulation $\mathcal{M}(\boldsymbol{x})$ is crucial. In particular, stress triaxiality is one of the most important factors in controlling such problems [48]. The stress triaxiality index provides useful insight into material performance under complex loading conditions. This helps in the design and optimization of structural components to improve performance and service life. By definition, stress triaxiality $\sigma_{\mathrm{ST}}(\boldsymbol{x})$ is the ratio of the hydrostatic stress $\sigma_{\mathrm{M}}(\boldsymbol{x})$ to a deformation-related deviatoric stress contribution $\sigma_{\mathrm{V}}(\boldsymbol{x})$. In mathematical terms,

$$\sigma_{\mathrm{ST}}(\boldsymbol{x}) = \frac{\sigma_{\mathrm{M}}(\boldsymbol{x})}{\sigma_{\mathrm{V}}(\boldsymbol{x})} \tag{2}$$

where, for general plane stress conditions, the hydrostatic stress corresponds to,

$$\sigma_{\mathrm{M}}(\boldsymbol{x}) = \frac{\sigma_{11}(\boldsymbol{x}) + \sigma_{22}(\boldsymbol{x})}{2} \tag{3}$$

where σ_{11} and σ_{22} are the principal stresses, and the deviatoric stress contribution can be considered as the equivalent von Mises stress,

$$\sigma_{\mathsf{V}}(\boldsymbol{x}) = \sqrt{\sigma_{11}^2(\boldsymbol{x}) + \sigma_{22}^2(\boldsymbol{x}) - \sigma_{11}(\boldsymbol{x})\sigma_{22}(\boldsymbol{x}) + 3\sigma_{12}^2(\boldsymbol{x})} \tag{4}$$

where $\sigma_{12}(\boldsymbol{x})$ is the shear stress.

If the analysis is performed in a 3D system, then the hydrostatic stress is equivalent to the following

$$\sigma_{\mathsf{M}}(\boldsymbol{x}) = \frac{1}{3}\mathrm{tr}\left(\boldsymbol{\sigma}(\boldsymbol{x})\right), \tag{5}$$

where $\boldsymbol{\sigma}$ is the Cauchy stress tensor.

In the same way, the equivalent von Mises stress corresponds to,

$$\sigma_{\mathsf{V}}(\boldsymbol{x}) = \left(\frac{1}{2}\left(\left(\sigma_{11}(\boldsymbol{x}) - \sigma_{22}(\boldsymbol{x})\right)^2 + \left(\sigma_{22}(\boldsymbol{x}) - \sigma_{33}(\boldsymbol{x})\right)^2 + \left(\sigma_{33}(\boldsymbol{x}) - \sigma_{11}(\boldsymbol{x})\right)^2 \right) + 3\left(\sigma_{12}^2(\boldsymbol{x}) + \sigma_{23}^2(\boldsymbol{x}) + \sigma_{31}^2(\boldsymbol{x})\right) \right)^{\frac{1}{2}}, \tag{6}$$

where σ_{33} is the principal stress, and σ_{23} and σ_{31} are the shear stresses.

Note that since it is assumed that the geometric properties of the system are affected by epistemic uncertainty, the stress triaxiality $\sigma_{\mathsf{ST}}(\boldsymbol{x})$ also depends on these geometric uncertainties, which are collected in the vector $\boldsymbol{x}$. Moreover, this uncertainty is also reflected in the von Mises $\sigma_{\mathsf{V}}(\boldsymbol{x})$ and hydrostatic $\sigma_{\mathsf{M}}(\boldsymbol{x})$ stresses. For example, consider a plate whose thickness varies along its domain. This variation can cause differences in hydrostatic stress at different locations, resulting in different magnitudes of stress triaxiality along the plate domain. In addition, if the plate has holes, inaccuracies in the shape, curvature, and location of the holes can cause stress concentration effects that change the stress state in the vicinity of the holes, thus varying the stress triaxiality.

Once the response of the system ($\sigma_{\mathsf{ST}}(\boldsymbol{x})$ for this work) and the n_x geometric uncertain parameters are identified, the next step is to characterize the uncertainty in those parameters. There are several techniques to characterize the uncertainty that affects stress triaxiality. One way is to resort to interval analysis following a set-based method. The next section discusses the essential definitions for incorporating this uncertainty using interval analysis.

3. Interval analysis

3.1. Interval theory

At an early design stage, the available data concerning the location of holes, thicknesses of elements, lengths, and shapes can be highly affected by epistemic uncertainty. In these cases, the source of uncertainty is due to a lack of knowledge produced by, for example, manufacturing processes, as was discussed in the previous sections. Typically, this data is not sufficient to build a robust numerical model to predict the behavior of mechanical components. One way to represent this type of uncertainty is to resort to interval analysis [24]. This technique has been extensively studied in finite element analysis to characterize the uncertainty in system input parameters (e.g., material properties and loading conditions) [49]. An interval or interval scalar is a convex subset of the domain of real numbers $\mathbb{R}$. An interval-valued parameter x^I is defined by,

$$x^I = [\underline{x}, \bar{x}] = \{x \in \mathbb{R} \mid \underline{x} \leq x \leq \bar{x}\} \tag{7}$$

where $\underline{x}$ represents the lower bound and $\bar{x}$ corresponds to the upper bound of x^I. Therefore, x^I contains all possible values that an uncertain input parameter can take, with no assumption made regarding the likelihood of those values [19]. For a better description of an interval quantity, the center or midpoint μ_{x^I} and the interval radius Δx^I are usually defined. The center of the interval is defined as,

$$\mu_{x^I} = \frac{\underline{x} + \bar{x}}{2} \tag{8}$$

and the interval radius corresponds to,

$$\Delta x^I = \frac{\bar{x} - \underline{x}}{2}. \tag{9}$$

In most cases, there is more than one uncertain parameter. In this situation, the definition of an interval vector is useful. An interval vector $\boldsymbol{x}^I$ is a vector in which each element is an interval,

$$\boldsymbol{x}^I = \begin{Bmatrix} x_1^I \\ x_2^I \\ \vdots \\ x_a^I \end{Bmatrix} = \left\{ \boldsymbol{x} \in \mathbb{R}^a \mid x_i \in x_i^I \right\} \tag{10}$$

with $\boldsymbol{x}^I \in \mathbb{IR}^a$, the domain of closed real-valued interval vectors of size a. Similarly, interval matrices are defined in $\mathbb{IR}^{a\times b}$ following the expression,

$$\boldsymbol{X}^I = \begin{Bmatrix} x_{11}^I & x_{12}^I & \cdots & x_{1b}^I \\ x_{21}^I & x_{22}^I & \cdots & x_{2b}^I \\ \vdots & \vdots & \ddots & \vdots \\ x_{a1}^I & x_{a2}^I & \cdots & x_{ab}^I \end{Bmatrix} = \left\{ \boldsymbol{X} \in \mathbb{R}^{a\times b} \mid x_{ij} \in x_{ij}^I \right\}. \tag{11}$$

In Eqs. (10) and (11), all indices in interval vectors and matrices are assumed to be independent. Consequently, an a-dimensional interval vector describes a hypercube in a-dimensional space. The lower and upper bounds of the interval scalar entries in the interval vector $\boldsymbol{x}^I$ determine the vertices of this hypercube [26,49].

3.2. Interval analysis

The basic idea of interval analysis is to search, from a hypercube $\boldsymbol{x}^I$ representing the uncertain input parameters, for those parameter realizations that yield the extreme response of the system [26]. If the n_x uncertain geometric parameters $\boldsymbol{x}$ of Eq. (1) are characterized through intervals (that is, $\boldsymbol{x}^I$), then the response of the system $\boldsymbol{y}$ will be approximated by the smallest hypercube $\boldsymbol{y}^I$. Typically $\boldsymbol{y}^I$ is calculated following a global optimization approach. In the case that the response of interest is scalar y^I, e.g. stress triaxiality (see Eq. (2)), the optimization problem corresponds to,

$$\underline{y} = \min_{\boldsymbol{x}\in\boldsymbol{x}^I} m(\boldsymbol{x}) \tag{12}$$

$$\bar{y} = \max_{\boldsymbol{x}\in\boldsymbol{x}^I} m(\boldsymbol{x}) \tag{13}$$

where $y^I = [\underline{y}, \bar{y}]$ is the interval response of the system which is defined by its lower $\underline{y}$ and upper $\bar{y}$ bounds. In the context of the global optimization approach (see e.g., [50,51]), repeated deterministic analyses are required to find the lower and upper bounds of the response, exploring various realizations of the uncertain geometric input parameters. Undoubtedly, the numerical cost associated with finding both bounds of the response is directly influenced by the nature of $m(\boldsymbol{x})$ and, hence, the response. If the response of the deterministic system varies monotonically concerning the uncertain parameters, the Vertex Method [52], ensures an exact result for optimizing the interval problem defined in Eqs. (12) and (13). On the contrary, if the behavior of m is non-monotonic, the accuracy of this approach quickly breaks down due to the limited number of sample points considered to find y^I [26]. For the cases where m is non-monotonic, the optimization procedure can be performed using black-box optimization routines [53,54] or surrogate models [55,56]. Note that the use of surrogate models helps to reduce the cost of finding $\underline{y}$ and $\bar{y}$. Nevertheless, the main challenge in this context is to build an accurate approximate response model, which can be quite difficult to achieve when the uncertainty is in the geometry.

The method used to construct $\mathcal{M}(\boldsymbol{x})$ also has a strong influence on the numerical cost of finding the response of interest (solution of Eqs. (12) and (13)). Especially when using the finite element method and considering that the uncertainty is in the geometry, it would be necessary to modify the discrete representation of the system (i.e. the mesh) for each of the realizations required to find the bounds of the response during the optimization stage. This disadvantage is caused by decoupling the meshing procedure and the numerical calculation of the field responses. One way to deal with this difficulty is to use a method that allows one to handle both geometry and solution fields simultaneously. The following section presents Isogeometric Analysis as a viable alternative for propagating geometric uncertainty.

4. Isogeometric analysis model

4.1. Structural response

The Isogeometric Analysis (IGA) was first proposed by Hughes et al. [28], as a means to parametrize the geometry associated with solid bodies analyzed using Finite Element Analysis (FEA). Both methods share basic ideas, however, in contrast to FEA, in IGA the geometry of the analyzed structure is not approximated by polynomial shape functions (e.g. Lagrangian basis functions) but described by a smooth geometry description used in Computer-Aided Design (CAD). Mostly, these descriptions are based on Non-Uniform Rational B-splines (NURBS). NURBS curves, surfaces, and volumes can be defined by knot vectors $\boldsymbol{\Xi}$ and control points. The knot vectors must have $n + p + 1$ increasing entries called knots ξ_i of the form

$$\boldsymbol{\Xi} = \left\{\xi_1, \xi_2, \ldots, \xi_{n+p+1}\right\}, \tag{14}$$

and define the parametric space as well as the NURBS order p. It also defines the C^{p-1-k} continuity conditions at the knots, where k denotes the number of repetitions of a specific knot in the knot vector $\boldsymbol{\Xi}$. Further, n is the total number of NURBS basis functions that are defined by,

$$R_{i,p}(\xi) = \frac{w_i N_{i,p}(\xi)}{W(\xi)}, \quad 1 \le i \le p+1, \quad \text{with} \quad W(\xi) = \sum_{i=1}^{\mathsf{n}_{\mathsf{cp}}} w_i N_{i,p}(\xi), \tag{15}$$

where n_{cp} is the total number of NURBS control points, $w_i > 0$ are weight factors and $N_{i,p}$ are B-spline basis functions of order p defined by the Cox-de Boor recursive formulas, cf. e.g. [30,39]. NURBS curves $\mathbf{C}(\xi)$ and surfaces $\mathbf{S}(\xi,\eta)$ are respectively described by,

$$\mathbf{C}(\xi) = \sum_{i=1}^{n} R_{i,p}(\xi)\mathbf{P}_i, \quad \mathbf{S}(\xi,\eta) = \sum_{i=1}^{n}\sum_{j=1}^{m} R_{i,p}(\xi)R_{j,q}(\eta)\mathbf{P}_{i,j}, \tag{16}$$

where $\mathbf{P}$ stores the control point coordinates, and m and q correspond to the number of NURBS basis functions, and the NURBS order in the second space dimension, respectively. Note that η represents a second parametric dimension (i.e. knots in the direction

of the second space dimension), which is collected in the knot vector $\mathbf{H}$. This knot vector $\mathbf{H}$ can be defined following Eq. (14). Note also that this description can be extended to define volumes, which requires the addition of a third parametric coordinate.

In this work, problems of linear elasticity are tackled, as introduced in Section 2. Similar to standard FEA formulations, the starting point to define the field responses is the Weak Form of Equilibrium

$$R(\mathbf{u},\mathbf{v}) = \int_{\Omega} \boldsymbol{\varepsilon}(\mathbf{u}) : \mathbb{C} : \boldsymbol{\varepsilon}(\mathbf{v})\,\mathrm{d}V - \int_{\Omega} \mathbf{b}\cdot\mathbf{v}\,\mathrm{d}V - \int_{\partial\Omega} \mathbf{t}\cdot\mathbf{v}\,\mathrm{d}A, \tag{17}$$

where $R(\mathbf{u},\mathbf{v})$ represents the residual form of the equilibrium equation, $\boldsymbol{\varepsilon}$ denotes the linear strain tensor, and $\mathbb{C}$ is the fourth order linear elasticity tensor. $\mathbf{u}$ and $\mathbf{v}$ are the displacement field and test function vectors (also known as virtual displacement field), and $\mathbf{b}$ and $\mathbf{t}$ are the body and traction force vectors, respectively. The physical space domain Ω is discretized using sub-domains called elements or knot-spans Ω_e that are defined in the parametric space $\bar{\Omega}$ by the structure of the knot vectors (i.e., $\boldsymbol{\Xi}$ and $\mathbf{H}$ in two-dimensional cases).

Element approximations of geometry $\mathbf{X}^h$, displacements $\mathbf{u}^h$ and test functions $\mathbf{v}^h$ read,

$$\mathbf{X}^h = \sum_{i=1}^{\mathsf{n}^{\mathsf{e}}_{\mathsf{cp}}} R_i(\xi,\eta)\mathbf{P}_i = \mathbf{N}\mathbf{P}_e, \quad \mathbf{u}^h = \sum_{i=1}^{\mathsf{n}^{\mathsf{e}}_{\mathsf{cp}}} R_i(\xi,\eta)\mathbf{u}_i = \mathbf{N}\mathbf{u}_e, \quad \mathbf{v}^h = \sum_{i=1}^{\mathsf{n}^{\mathsf{e}}_{\mathsf{cp}}} R_i(\xi,\eta)\mathbf{v}_i = \mathbf{N}\mathbf{v}_e, \tag{18}$$

where $R_i(\xi,\eta) \equiv R_{i,p}(\xi)R_{j,q}(\eta)$, $\mathbf{N}$ is the matrix of shape functions, and $\mathsf{n}^{\mathsf{e}}_{\mathsf{cp}}$ is the number of control points of an element Ω_e. $\mathbf{P}_e$, $\mathbf{u}_e$, and $\mathbf{v}_e$ are the control point matrix, displacements, and test functions, per element, respectively.

Using this matrix notation, the symmetric linear strains can be approximated by,

$$\boldsymbol{\varepsilon}(\mathbf{u}^h) = \sum_{i=1}^{\mathsf{n}^{\mathsf{e}}_{\mathsf{cp}}} \mathbf{B}_i\mathbf{u}_i = \mathbf{B}\mathbf{u}_e \quad \text{and} \quad \boldsymbol{\varepsilon}(\mathbf{v}^h) = \sum_{i=1}^{\mathsf{n}^{\mathsf{e}}_{\mathsf{cp}}} \mathbf{B}_i\mathbf{v}_i = \mathbf{B}\mathbf{v}_e, \tag{19}$$

with the strain–displacement matrix $\mathbf{B}$ and the matrix of shape functions $\mathbf{N}$ given by,

$$\mathbf{B} = \begin{bmatrix} R_{1,x} & 0 & \dots & R_{\mathsf{n}^{\mathsf{e}}_{\mathsf{cp}},x} & 0 \\ 0 & R_{1,y} & \dots & 0 & R_{\mathsf{n}^{\mathsf{e}}_{\mathsf{cp}},y} \\ R_{1,y} & R_{1,x} & \dots & R_{\mathsf{n}^{\mathsf{e}}_{\mathsf{cp}},x} & R_{\mathsf{n}^{\mathsf{e}}_{\mathsf{cp}},x} \end{bmatrix} \quad \text{and} \quad \mathbf{N} = \begin{bmatrix} R_1 & 0 & \dots & R_{\mathsf{n}^{\mathsf{e}}_{\mathsf{cp}}} & 0 \\ 0 & R_1 & \dots & 0 & R_{\mathsf{n}^{\mathsf{e}}_{\mathsf{cp}}} \end{bmatrix}. \tag{20}$$

It is important to highlight that the discretized matrix form of the weak equilibrium equation (see Eq. (17)) only differs from the FEA formulation by the choice of the shape functions, viz.

$$R_e = \mathbf{v}_e^{\mathsf{T}}\mathbf{R}_e = \mathbf{v}_e^{\mathsf{T}}\left[\int_{\Omega_e} \mathbf{B}^{\mathsf{T}}\mathbf{C}\mathbf{B}\,\mathrm{d}V\ \mathbf{u}_e - \int_{\Omega_e} \mathbf{N}^{\mathsf{T}}\mathbf{b}\,\mathrm{d}V - \int_{\partial\Omega_e} \mathbf{N}^{\mathsf{T}}\mathbf{t}\,\mathrm{d}A\right] = \mathbf{v}_e^{\mathsf{T}}\left[\mathbf{K}_e\mathbf{u}_e - \mathbf{f}_e\right], \tag{21}$$

where R_e is the residual of the elemental equilibrium equation, $\mathbf{R}_e$ represents the elemental internal force vector, and $\mathbf{C}$ is the constitutive matrix, which characterizes the material properties.

Assembling all elements and identifying the first integral of Eq. (21) as the element stiffness matrix $\mathbf{K}_e$, and the other two as element force vector $\mathbf{f}_e$, and excluding the trivial solution $\mathbf{v} = \mathbf{0}$, the discrete system of equations for solving the solution of the displacements reads,

$$\bigcup_{e=1}^{\mathsf{n}_{\mathsf{el}}} \left[\mathbf{K}_e\mathbf{u}_e - \mathbf{f}_e\right] = \mathbf{K}\mathbf{u} - \mathbf{F} = \mathbf{0}, \tag{22}$$

where $\bigcup_{e=1}^{\mathsf{n}_{\mathsf{el}}}$ represents a union operation over all n_{el} elements in the discretized domain, $\mathbf{K}$ is the stiffness matrix of the system, $\mathbf{F}$ is the force vector, and $\mathbf{u}$ the displacement. It is noteworthy that, unlike FEA, in IGA the response in displacements is given in the positions of the control points. With the solution of Eq. (22) any response function of interest can be computed within a post-processing step similar to FEA [29]. In this study, the so-called stress triaxiality is focused, cf. Eq. (2). To provide a clearer understanding of how the system's response is obtained at control points, Fig. 1 illustrates the key domains involved in integration in the IGA process, emphasizing the transition from the physical domain to the parametric and parent domains (red arrows in the figure). Fig. 1 first shows the physical domain in light blue, which represents the actual geometry of the system under study. For real-world problems, this domain is often complex and may include curved shapes, as shown in the figure. Within this domain, an element Ω_e is highlighted in orange to indicate the current region where the analysis is being performed. Note that given the definition of the control points and knot vectors, four elements are used to represent the system. Also, note that the control points are not necessarily part of physical space. Moreover, observe that the control points are connected by the control mesh. The physical domain is then mapped onto the parametric domain (see element $\bar{\Omega}_e$). Unlike traditional FEA where the physical space is directly discretized, IGA relies on this intermediate parametric space. The parametric domain is structured in a grid format defined by knot-related coordinates. The dimensions and continuity of this space are determined by the associated knot vectors and the order p of the NURBS, as shown in Eqs. (14) and (15). This parametric domain plays a critical role in the IGA process because it allows for the accurate representation of elements within the physical domain using NURBS-based shape functions. Finally, the elements within the parametric domain are further mapped to the parent domain, a standardized space commonly used in FEA. The solution of the PDE is ultimately obtained at the knots within the parametric domain and then mapped back into physical space. For this mapping, it is necessary to construct a mesh in physical space for visualization purposes. Furthermore, using post-processing techniques, like in FEA, it is possible to obtain the desired response of interest [30]. A detailed explanation of the mappings used to integrate in Isogeometric Analysis can be found in [28]. It is important to note that while mesh refinement techniques exist within the IGA framework, they are beyond the scope of this study and are not explored in this work.

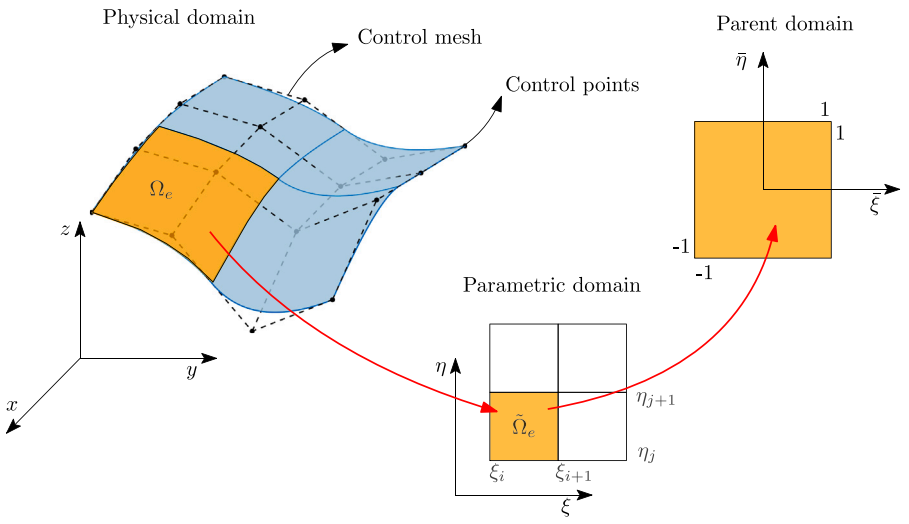

Fig. 1. Domains used for integration in Isogeometric Analysis.

Since the objective of this work is to apply a gradient-based optimization scheme to propagate efficiently the geometric uncertainties during the interval analysis, the next subsection discusses the procedure to obtain the sensitivities of the response.

4.2. Geometric sensitivity analysis

Design sensitivity analysis helps to quantify the change of any response function $f(\mathbf{u}(\boldsymbol{x}), \boldsymbol{x})$, e.g. stress or strain measures, concerning alterations in chosen design (uncertain) parameters $\boldsymbol{x}$. In the following, the sensitivity relations are derived for the depicted linear elastic model, with respect to the model geometry $\mathbf{X}$. By employing variational sensitivity analysis, as discussed in e.g. [42,57], this change can be expressed as

$$\delta f = \delta_u f + \delta_X f = \left[\frac{\partial f}{\partial \mathbf{u}}\right] \delta\mathbf{u} + \left[\frac{\partial f}{\partial \mathbf{X}}\right] \delta\mathbf{X}. \tag{23}$$

Following the direct differentiation method (DDM), Eq. (22) has to hold for any design variation $\delta\mathbf{X}$, i.e. forcing a design change to satisfy the weak equilibrium condition resulting in its vanishing total variation

$$\delta R(\mathbf{u}, \mathbf{v}, \delta\mathbf{u}, \delta\mathbf{X}) = \delta_u R(\mathbf{u}, \mathbf{v}, \delta\mathbf{u}) + \delta_X R(\mathbf{u}, \mathbf{v}, \delta\mathbf{X}) = 0. \tag{24}$$

Using the same discretization concepts as described above, both variations in Eq. (24) can be approximated by

$$\delta_u R(\mathbf{u}, \mathbf{v}, \delta\mathbf{u}) \approx \delta_u R(\mathbf{u}^h, \mathbf{v}^h, \delta\mathbf{u}^h) = \mathbf{v}^\mathsf{T} \mathbf{K}\, \delta\mathbf{u} \tag{25}$$

and

$$\delta_X R(\mathbf{u}, \mathbf{v}, \delta\mathbf{X}) \approx \delta_X R(\mathbf{u}^h, \mathbf{v}^h, \delta\mathbf{X}^h) = \mathbf{v}^\mathsf{T} \mathbf{Q}\, \delta\mathbf{P}. \tag{26}$$

Here, $\mathbf{K}$ denotes the global stiffness matrix, cf. Eq. (22), $\mathbf{P}$ is the control points matrix, and $\mathbf{Q}$ is the global pseudo-load matrix that can be derived to

$$\mathbf{Q} = \bigcup_{e=1}^{n_{el}} \mathbf{Q}_e = \bigcup_{e=1}^{n_{el}} \int_{\Omega_e} \sum_i \sum_j \left[\boldsymbol{\sigma}(\mathbf{L}_i \mathbf{L}_j^\mathsf{T} - \mathbf{L}_j \mathbf{L}_i^\mathsf{T}) - \mathbf{B}_i^\mathsf{T} \mathbf{C} \mathbf{B}_j \mathbf{H}\right] \mathrm{d}V, \tag{27}$$

where $\mathbf{Q}_e$ corresponds to the element pseudo-load matrix and $\mathbf{H}$ represents the approximation of the element displacement gradient. Further, $\mathbf{L}_i$ is the column matrix of shape function derivatives for the ith control point, viz.

$$\mathbf{H} = \nabla \mathbf{u}_e = \sum_i^{n_{cp}^e} \mathbf{u}_i \mathbf{L}_i^\mathsf{T} \quad \text{and} \quad \mathbf{L}_i = \begin{bmatrix} R_{i,x} & R_{i,y} \end{bmatrix}^\mathsf{T}. \tag{28}$$

Here, n_{cp}^e denotes the number of control points of the element e. For a detailed derivation of Eqs. (23)–(28), the interested reader is referred to e.g. [58]. Again, excluding the trivial solution $\mathbf{v} = \mathbf{0}$, the total response sensitivity matrix $\mathbf{S}$ can be identified by rearranging the discrete total variation of the weak equilibrium condition

$$\mathbf{K}\delta\mathbf{u} = -\mathbf{Q}\,\delta\mathbf{P} \quad \Rightarrow \quad \delta\mathbf{u} = -\mathbf{K}^{-1}\mathbf{Q}\,\delta\mathbf{P} = \mathbf{S}\,\delta\mathbf{P}. \tag{29}$$

With the above-described variational method, the discrete sensitivity relation of the stress triaxiality can be expressed by

$$\delta\sigma_{\mathrm{ST}} = \left[\frac{\partial\sigma_{\mathrm{ST}}}{\partial\sigma_{\mathrm{M}}}\frac{\partial\sigma_{\mathrm{M}}}{\partial\boldsymbol{\sigma}} + \frac{\partial\sigma_{\mathrm{ST}}}{\partial\sigma_{\mathrm{V}}}\frac{\partial\sigma_{\mathrm{V}}}{\partial\boldsymbol{\sigma}}\right]\delta\boldsymbol{\sigma}. \tag{30}$$

Here, the computation of the partial derivatives is straightforward. According to Eq. (23) together with Eq. (29), the total variation of the stress tensor reads

$$\delta\boldsymbol{\sigma} = \left[\frac{\partial\boldsymbol{\sigma}}{\partial\mathbf{u}}\mathbf{S} + \frac{\partial\boldsymbol{\sigma}}{\partial\mathbf{P}}\right]\delta\mathbf{P}. \tag{31}$$

It should be noted that not all control point coordinates are necessarily selected as design variables. In specific cases, it may be advantageous to identify a parameterization that allows for the definition of sensitivity relations e.g. regarding some geometric parameters such as lengths and radii. In these cases, a projection of the above-derived sensitivity equations utilizing a design-velocity matrix $\mathbf{D}$ of the form

$$\delta\mathbf{P} = \mathbf{D}\,\delta\boldsymbol{x} \tag{32}$$

is useful, where $\boldsymbol{x}$ denote the aforementioned uncertain geometric parameters of interest. With this definition in Eq. (32), the projection of Eq. (31) reads

$$\delta\boldsymbol{\sigma} = \left[\frac{\partial\boldsymbol{\sigma}}{\partial\mathbf{u}}\mathbf{S} + \frac{\partial\boldsymbol{\sigma}}{\partial\mathbf{P}}\right]\mathbf{D}\,\delta\boldsymbol{x}. \tag{33}$$

Observe how now the total variation of the stress tensor takes into account the derivatives with respect to the uncertain parameters. The described isogeometric model has been implemented in `MatLab` utilizing the NURBS toolbox, cf. [59] and the formulations mostly follow those described in [30].

5. Proposed strategy for uncertainty propagation

5.1. General remarks

The previous section defined Isogeometric Analysis (IGA) as a powerful tool for determining field responses in a numerical model using the same basis functions that define the geometry. Additionally, it described how to compute the sensitivities of these field responses concerning uncertain parameters through a variational formulation. To use IGA for propagating geometric uncertainties characterized as interval variables, it is crucial to strategically define the locations of control points based on geometric parameters such as radius, thickness, length, etc. This approach is effective because, in IGA with variational formulation, the system response and sensitivities are obtained simultaneously at the control points. Nevertheless, the control points are not necessarily located within the actual geometry of the system (as shown in Fig. 1). Therefore, when calculating the response and sensitivities, it is necessary to map them from being functions of the control points (see Eq. (31)) to being functions of the uncertain geometric parameters (see Eq. (33)). Note that this assumes that the response and its sensitivities have already been calculated at the location of the control points, as explained in Section 4. For a comprehensive description of this procedure, the reader is referred to [29,30]. Once the sensitivities with respect to the control points are mapped to depend on the uncertain parameters, this information can be used to perform the optimization for the interval analysis, i.e., to find the lower (Eq. (12)) and upper (Eq. (13)) bounds of the response. This procedure is described in the next subsection.

5.2. Gradient-based optimization

Section 3.2 explained that interval analysis attempts to find the bounds of the response of interest, given the characterization of uncertain geometric parameters as intervals. One way to find these bounds is to use a gradient-based algorithm. Gradient-based optimization (GBO) is a widely used method for finding the minimum or maximum of a function by iteratively descending based on the direction of the gradient [41]. In this work, since information on the sensitivity of the response concerning uncertain parameters is available, this method seems appropriate for interval analysis. The GBO scheme used in this paper corresponds to the trust-region algorithm [60]. The trust-region algorithm in `MatLab` approximates the objective function with a simpler model within a neighborhood called the trust region. It often uses Sequential Quadratic Programming (SQP) techniques to solve the trust-region subproblem, which involves minimizing a quadratic model subject to a constraint within the trust region. The gradient information is crucial in this process, as it helps in the construction of the quadratic model and guides the direction of the search. The algorithm ensures robust convergence, especially for nonlinear optimization problems, by iteratively updating the size of the confidence region based on the accuracy of the model [61].

5.3. Summary of the proposed strategy

The following steps, which are also shown in Fig. 2, summarize the proposed methodology for performing an Isogeometric Analysis considering that the uncertainty in the geometry is represented by intervals.

1. Define the numerical model (Eqs. (1) and (22)) and the response of interest (Eq. (2)).

2. Identify the uncertain geometric parameters $\boldsymbol{x}$ of the model.
3. Define the uncertainty in the geometric parameters using intervals $\boldsymbol{x}^{\boldsymbol{I}}$ (Eq. (10)).
4. Set the control point matrix $\mathbf{P}$ according to the desired geometry, in terms of the uncertain geometric parameters $\boldsymbol{x}$.
5. Compute the sensitivities of the control points matrix concerning the uncertain geometric parameters, i.e. compute the design-velocity matrix $\mathbf{D}$.
6. Set up the NURBS associated with the model: curves, surfaces, and volumes (Eq. (16)).
7. Apply gradient-based optimization to define the lower $\underline{y}$ and upper $\bar{y}$ bounds of the response.

   (a) Perform Isogeometric Analysis (IGA) to calculate the response of interest (Eq. (2)) and its sensitivities (Eq. (30)) using a variational analysis, i.e., compute the response and sensitivities at the control points.
   (b) Post-process IGA response and obtain sensitivities depending on geometric uncertain parameters $\boldsymbol{x}$ (Eq. (33)) using the sensitivities calculated in 5.

Note that the sequence of steps 5 and 6 is not mandatory and can be performed in any order. The sensitivities calculated in Step 5 depend on the parametric definition of the control point matrix $\mathbf{P}$ and are unaffected by the subsequent NURBS model setup in Step 6. However, the existing order is maintained for logical clarity and to facilitate the gradient-based optimization process in Step 7.

6. Illustrative examples

6.1. 2D linear hook

The proposed methodology is applied to estimate the maximum stress triaxiality of a linear two-dimensional steel hook system. The base end of the hook is fixed and a load of 20 kN is applied to the top end. The material properties of the hook system are assumed deterministic and equal to $E = 2{\times}10^5\,\mathrm{N/mm^2}$ for Young's modulus and $\nu = 0.3$ for Poisson's ratio. The plane stress conditions are assumed. Regarding the geometry of the system, it is assumed that the value of the radius and thickness are uncertain due to the lack of knowledge at the early design stage. These geometric quantities are characterized by the intervals $r^I = [10, 50]$ mm and $t^I = [15, 40]$ mm, for the radius and thickness, respectively. Note that these wide ranges are defined to emphasize the high degree of uncertainty that can exist at this design stage. Fig. 3 shows the IGA model for the stress triaxiality analysis. Note that in this figure, the geometry representation is schematized considering the midpoints of the intervals, that is, $\mu_{r^I} = 30$ mm and $\mu_{t^I} = 27.50$ mm.

The NURBS surface used to represent the hook system is constructed based on $\mathsf{n}_{\mathsf{cp}} = 6$ control points (see Fig. 3). To translate the uncertainty in the geometric input parameters to NURBS control point's matrix $\mathbf{P}$, a parametric representation of the coordinates of each control point in terms of r and t is proposed

$$\mathbf{P} = \begin{bmatrix} t & 0 \\ t & r \\ t+r & r \\ 0 & 0 \\ 0 & t+r \\ t+r & t+r \end{bmatrix}. \tag{34}$$

It is important to note that to compute sensitivities using the variational approach of Section 4.2, the partial derivatives of the control point matrix $\mathbf{P}$ with respect to r and t must also be computed, as shown in Eq. (32) and explained in Section 4.2. This is necessary to map the sensitivities from the control points to the uncertain parameters. For this task, the corresponding design-velocity matrix $\mathbf{D}$ must be computed. By collecting all elements of the matrix $\mathbf{P}$ in a column vector, where the coordinates of each control point are written sequentially, the design-velocity matrix is equal to

$$\mathbf{D} = \begin{bmatrix} 0 & 0 & 0 & 1 & 1 & 1 & 0 & 0 & 0 & 1 & 1 & 1 \\ 1 & 0 & 1 & 0 & 1 & 0 & 0 & 0 & 0 & 1 & 1 & 1 \end{bmatrix}^{\mathsf{T}}. \tag{35}$$

Note that each column of the design-velocity matrix $\mathbf{D}$ contains the derivatives of all coordinates of the control points with respect to each geometric uncertain parameter considered. For the definition of the NURBS surface, quadratic elements with overlapping (elements can share control points or knots) are considered. The polynomial degree p of the splines associated with the knot vector in the $x-$direction is two, while in the $y-$direction is one. On the other hand, the multiplicity of the knots k is one and zero for the $x-$direction and the $y-$direction, respectively. For both directions, the weights $w = [1, \frac{1}{\sqrt{2}}, 1]$ are associated with the control points of the inner and outer curves that allow to represent the hook geometry.

Since this study aims to determine the variation of the maximum stress triaxiality σ_{ST} in the hook system, a gradient-based optimization approach is used to determine its lower and upper bounds. The initial point for the optimization scheme was considered as $\boldsymbol{x}_0 = [\mu_{r^I}, \mu_{t^I}]$. The results were compared by considering the Vertex Method (VM) [52], Particle Swarm Optimization (PSO) [62], Surrogate Optimization (SO) using the Radial Basis Function (RBF) interpolation algorithm available in `Matlab` [63], and Pattern

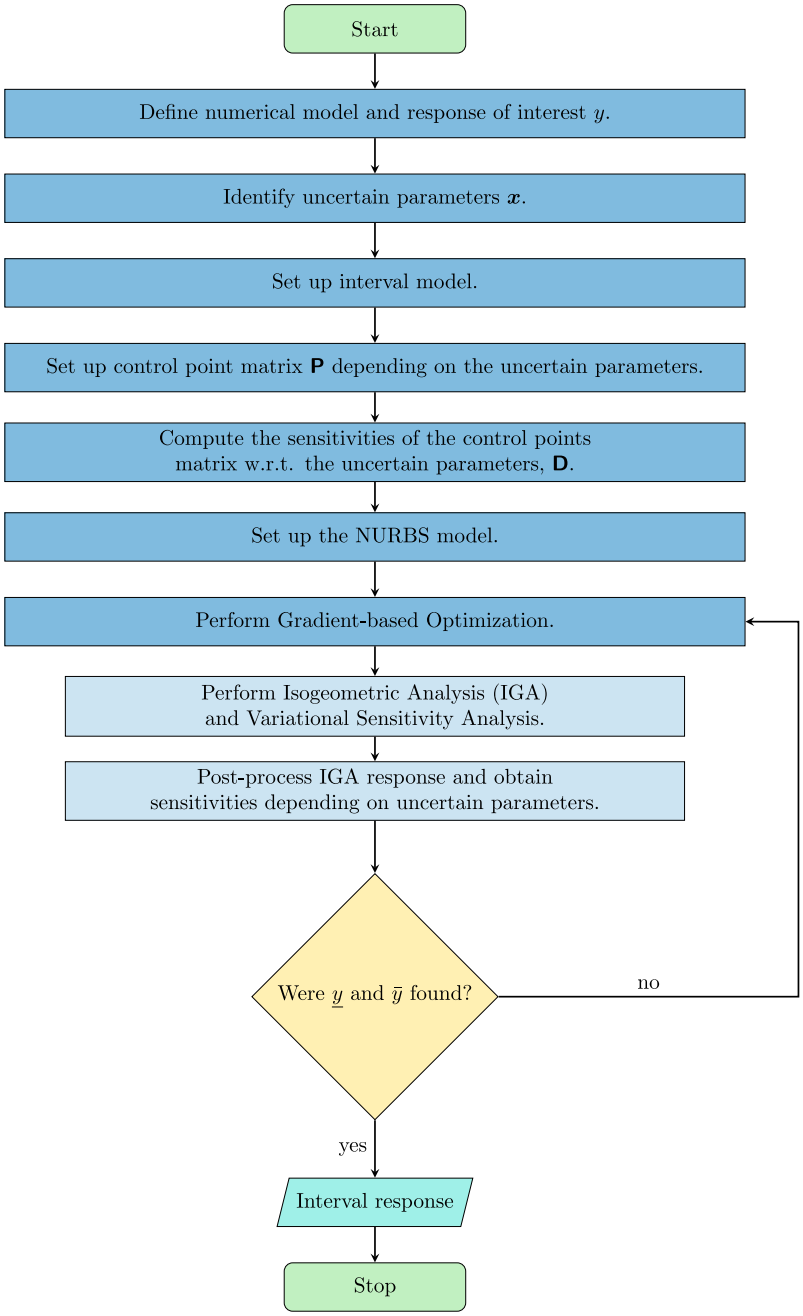

Fig. 2. Flowchart of Isogeometric Analysis for quantifying geometric uncertainties characterized by intervals.

Search Optimization (PS) [64]. Table 1 shows the results for the lower bound of the maximum stress triaxiality of the hook system. Note that all evaluated methods identify the lower bound of the maximum response $\max(\sigma_{ST}) = 0.4420$ for a radius equal to $r = 10\,\text{mm}$ and a thickness of $t = 40\,\text{mm}$. However, the Gradient-based Optimization (GBO) method appears to be the most efficient, after the Vertex Method (VM), requiring only five deterministic analyses of the hook system to identify this lower bound, highlighting the numerical advantage of the proposed strategy. It should be noted that although the VM leads to the exact results in this example (for the lower bound of the maximum stress triaxiality), this method is only accurate for cases where the response behaves monotonically over the search space. Therefore, it is recommended to use it as a reference, but one should be aware that it may underestimate the bounds of the response. It is also important to note that the numerical cost of VM increases as a function of the number of uncertain parameters.

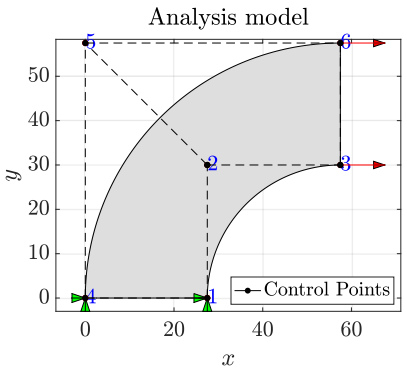

Fig. 3. Hook 2D model for stress triaxiality analysis. The geometry considered corresponds to that described by the midpoints of the intervals associated with radius and thickness.

Table 1
Results of optimization – lower bound of maximum stress triaxiality – Hook 2D.

Method	r in mm	t in mm	max(σ_{ST})	No. analysis
Vertex Method (VM)	10	40	0.4420	4
Particle Swarm Optimization (PSO)	10	40	0.4420	2254
Surrogate Optimization (SO)	10	40	0.4420	200
Pattern Search Optimization (PS)	10	40	0.4420	62
Gradient-based Optimization (GBO)	10	40	0.4420	5

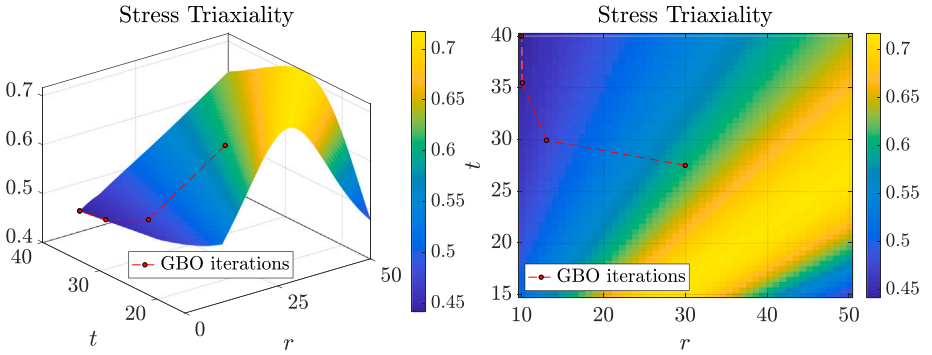

(a) Maximum stress triaxiality as a function of geometric parameters.

(b) GBO iterations.

Fig. 4. Distribution of the maximum stress triaxiality over the search space and iterations performed for the GBO algorithm to find the lower bound. r and t in mm.

In the hook example, only two uncertain parameters are considered. This allows the behavior of the maximum stress triaxiality within the search space to be visualized. As shown in Fig. 4.a, the maximum stress triaxiality is plotted as a function of the geometric parameters under consideration. Simultaneously, Fig. 4.b shows the iterations performed for the GBO approach. The first observation to be made is that the response does not exhibit monotonic behavior concerning both radius and thickness. Consequently, it is expected that the VM may produce inaccurate results when finding the upper bound of the response, whereas the accurate result of VM for the lower bound can only be explained by the fact that the lower bound is located in a corner of the search space. The second observation concerns the availability of information about the sensitivity of the response. This information facilitates the rapid convergence of the algorithm to the optimal value. This is an indication of the efficiency and effectiveness of the GBO approach in this context.

The resulting geometry for the hook system with the optimum values of radius and thickness for the lower bound of the response is shown in Fig. 5.a. As expected, the lower limit of maximum stress triaxiality is associated with a thicker hook geometry. Fig. 5.b shows the deformed shape due to the force applied at the right end of the hook, while Figs. 5.c and 5.d show the stress triaxiality distribution over the original and deformed hook shapes, respectively. Note that the maximum values of stress triaxiality are located in the outer curve of the hook. These areas of higher stress triaxiality (closer to 0.4) are likely to be more susceptible to failure under load because they indicate a high concentration of stress.

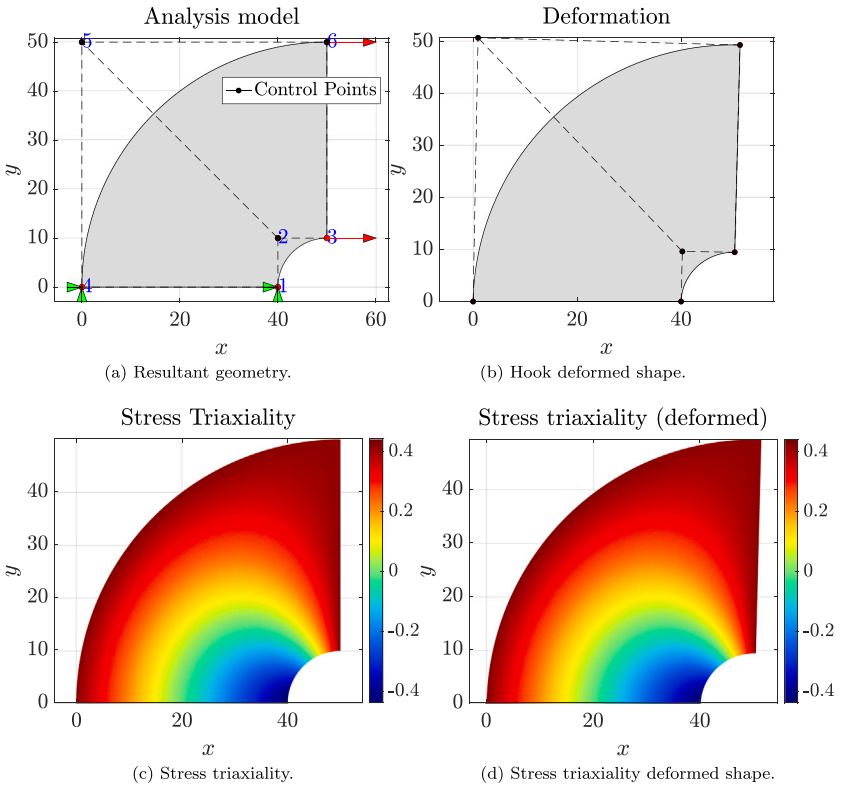

(a) Resultant geometry. (b) Hook deformed shape.

(c) Stress triaxiality. (d) Stress triaxiality deformed shape.

Fig. 5. Resultant geometry and stress triaxiality for the lower bound results. Dimensions in mm.

Table 2
Results of optimization – upper bound of maximum stress triaxiality – Hook 2D.

Method	r in mm	t in mm	$\max(\sigma_{ST})$	No. analysis
Vertex Method (VM)	50	40	0.6380	4
Particle Swarm Optimization (PSO)	49.6141	26.7778	0.7170	3803
Surrogate Optimization (SO)	47.4384	25.6038	0.7170	200
Pattern Search Optimization (PS)	49.0995	26.5000	0.7170	149
Gradient-based Optimization (GBO)	36.0834	19.4750	0.7170	8

Table 2 shows the results of the optimization procedure for the upper bound of the maximum stress triaxiality. For this bound, it is clear that the Vertex Method underestimates the optimum, which can be observed in Fig. 6 due to the non-monotonicity of the maximum stress triaxiality response. Note that all optimization methods used to find the upper bound of $\max(\sigma_{ST})$, obtain the same optimal value of maximum stress triaxiality by different radius and thickness combinations. This is due to the flat behavior of stress triaxiality over the search space observed in Fig. 6. In the same way, as for the lower bound of the response, the GBO method appears to be the most efficient, requiring only eight deterministic analyses of the system.

Fig. 7.a shows the resulting geometry for the hook system with the optimum values of radius and thickness for the upper bound of the response. A thinner hook geometry is associated with the upper bound of the maximum stress triaxiality. Fig. 7.b shows the deformed geometry resulting from the force applied to the right end of the hook, while Figs. 7.c and 7.d show the stress triaxiality distribution over the original and deformed hook geometry, respectively. Note that, as observed for the lower bound results, the maximum values of stress triaxiality are located in the outer curve of the hook. Again, these areas of higher stress triaxiality (closer to 0.7) are likely to be more susceptible to failure under load. Unlike the resulting geometry for the lower boundary, a wider range of stress triaxiality values is now observed in the hook shape.

6.2. Solid horseshoe

The second example illustrates a geometrically complex but single-patch three-dimensional horseshoe problem adapted from [28, 65]. The objective of the study is to estimate the maximum stress triaxiality in the horseshoe shape subjected to equal and opposite

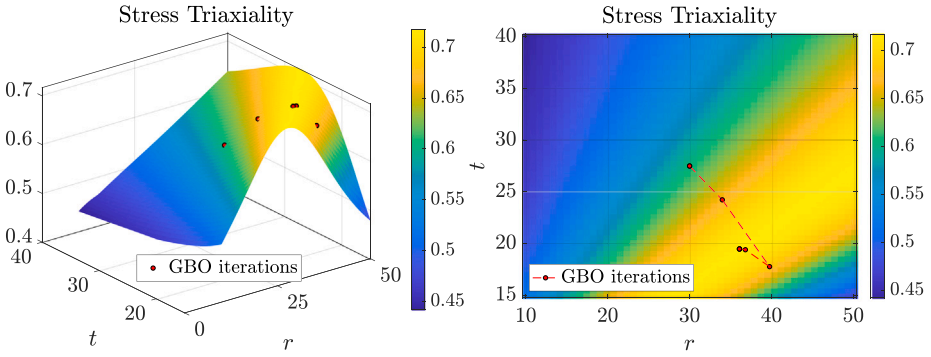

(a) Maximum stress triaxiality as a function of geometric parameters.

(b) GBO iterations.

Fig. 6. Distribution of the maximum stress triaxiality over the search space and iterations performed for the GBO algorithm to find the upper bound. r and t in mm.

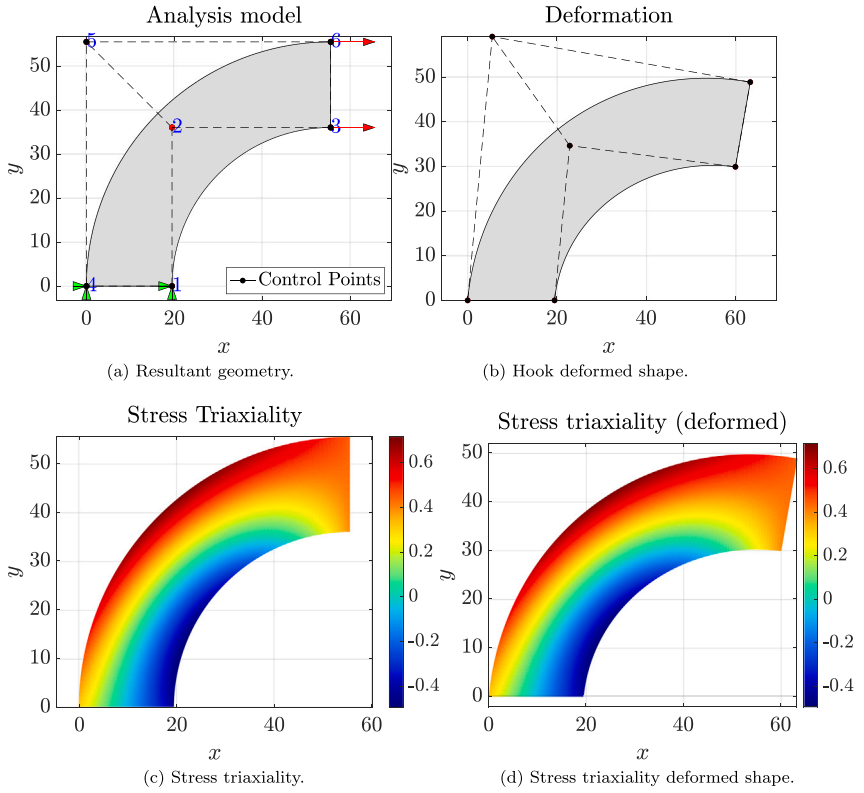

(a) Resultant geometry.

(b) Hook deformed shape.

(c) Stress triaxiality.

(d) Stress triaxiality deformed shape.

Fig. 7. Resultant geometry and stress triaxiality for the upper bound results. Dimensions in mm.

in-plane flat-edge unitary displacements (see Fig. 8). The base ends of the horseshoe are fixed in the $y-$direction, while only the outer corners are fixed in the $z-$direction. In the $x-$direction, there is a deterministic prescribed unitary displacement $-u_0$ for the left side (non-positive $x-$coordinates), while there is a deterministic prescribed unitary displacement u_0 for the right side (positive $x-$coordinates). Furthermore, the displacements in the $x-$direction are also restricted at the center of the top of the horseshoe. The material properties of the horseshoe system are assumed to be deterministic and equal to $E = 3 \times 10^7\ \mathrm{N/cm^2}$ for Young's modulus and $\nu = 0.3$ for Poisson's ratio. The geometry of the horseshoe is constructed by performing a U-sweep on the cross-section of a

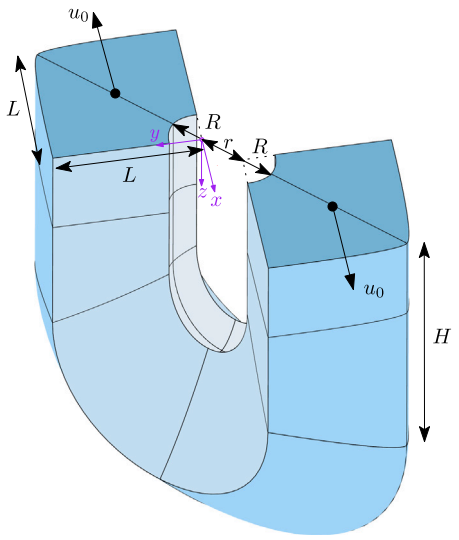

Fig. 8. Uncertain geometric parameters of solid horseshoe 3D model for stress triaxiality analysis.

square of dimensions $L \times L$, subtracted by a quarter disk of radius R, which defines the inner edge. The outer edge has a slightly rounded end defined by the value of L. The horseshoe definition includes a straight portion of height H, and the distance between the origin and the center of the quarter disk is defined by r (see Fig. 8). It is assumed that the values of the parameters that define the geometry L, R, r, and H are uncertain due to lack of knowledge at the early design phase. These geometric quantities are defined by the intervals $L^I = [3.5, 5.5]$, $R^I = [0.5, 1.5]$, $r^I = [0.9142, 1.9142]$, and $H^I = [7.5, 8.5]$ in cm. Fig. 9 shows the IGA model for stress triaxiality analysis in the horseshoe, where the geometry representation, as in the hook example, is defined by the midpoints of the interval variables.

The NURBS volume used to represent the horseshoe-shaped geometry is based on $\mathsf{n}_{\mathsf{cp}} = 108$ control points, which comprises 324 degree-of-freedom. A parametric representation of the coordinates of each control point in terms of L, R, r, and H is proposed to translate the uncertainty in the geometric input parameters into the NURBS control point matrix. As can be seen in Fig. 9, the control points are strategically placed to achieve the desired curvature and smoothness. To create the NURBS of the horseshoe, the area of its cross-section was modeled using three curves: an inner curve (representing the edge created by extracting the quarter disk of radius R), an outer curve (the opposite side of the extracted quarter disk), and a curve located between the inner and outer curves. Each curve is composed of four control points where, depending on the desired curvature, the weights $w_1 = 0.8536$, $w_2 = 0.7071$, $w_3 = 0.6036$, and $w_4 = 1$ were used. These sections were repeated at different heights: $z = 0, \frac{H}{4}, \frac{H}{2}$, for the straight section of the horseshoe, for both ends. Three cross-section areas were used to define the curved portion of the horseshoe. Two of them replicated the cross-section with an inclination of 45 degrees with respect to the plane $z = H$ for the left and right side, while the third one was located in the center of the horseshoe geometry with an inclination of 90 degrees with respect to the plane $z = H$. The resulting NURBS volume is composed of displacement-based solid elements. The polynomial degree p of the splines that are associated with the knot vectors is three for the x, y, and $z-$dimension. The knot vectors used to define the parametric space are:

$$\boldsymbol{\Xi} = \{0,0,0,\frac{1}{2},1,1,1\},\ \mathbf{H} = \{0,0,0,1,1,1\},\ \mathbf{Z} = \{0,0,0,\frac{1}{6},\frac{2}{6},\frac{1}{2},\frac{1}{2},\frac{4}{6},\frac{5}{6},1,1,1\}. \tag{36}$$

The lower and upper bounds of the maximum stress triaxiality σ_{ST} in the horseshoe system are determined using a gradient-based optimization approach, taking advantage of the sensitivities computed along with the IGA model. The starting point for the optimization scheme was considered as $\boldsymbol{x}_0 = [\mu_{L^I}, \mu_{R^I}, \mu_{r^I}, \mu_{H^I}]$. The results were compared by considering the Vertex Method (VM) [52], Particle Swarm Optimization (PSO) [62], Surrogate Optimization (SO) using the Radial Basis Function (RBF) interpolation algorithm available in `Matlab` [63], and Pattern Search Optimization (PS) [64], similar to the first example. Table 3 shows the results for the lower bound of the maximum stress triaxiality of the solid horseshoe. The geometric parameters (R, r, L, H) are also listed for each method, along with the number of deterministic analyses performed. While VM requires the least number of analyses (16), it underestimates the lower bound of the stress triaxiality, reflecting a non-monotonic behavior of the response of interest with respect to the uncertain parameters. It is important to note that in this example, due to the number of uncertain parameters considered in the analysis, it is not possible to visualize the behavior of the stress triaxiality in the search space as it was possible in the first example. Regarding the results obtained by the applied optimization schemes, PSO, SO, and PS achieve the smaller value for the lower bound; however, PSO requires a significantly higher computational effort of 4797 analyses, making it less efficient. Overall, GBO provides the best balance between accuracy and computational complexity, requiring only 26 analyses.

The resulting geometry for the horseshoe system with the optimal values of the uncertain parameters for the lower bound of the response is shown in Fig. 10.a. As expected, the lower limit of the maximum stress triaxiality is associated with a thicker section

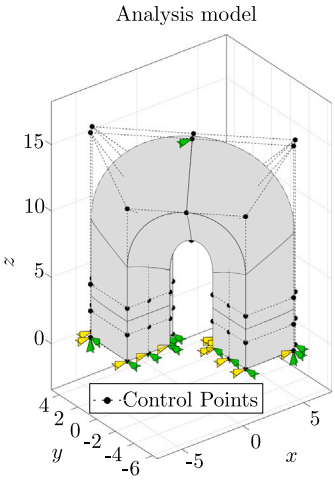

Fig. 9. Solid horseshoe 3D model for stress triaxiality analysis. The geometry considered corresponds to that described by the midpoints of the intervals associated with the uncertain parameters. Dimensions in cm.

Table 3
Results of optimization – lower bound of maximum stress triaxiality – Horseshoe 3D.

Method	R in cm	r in cm	L in cm	H in cm	$\max(\sigma_{ST})$	No. analysis
Vertex Method (VM)	0.5000	0.9142	3.5000	8.5000	3.3271	16
Particle Swarm Optimization (PSO)	0.5000	0.9142	4.5328	8.5000	3.3186	4797
Surrogate Optimization (SO)	0.5000	0.9142	4.5327	8.4996	3.3186	200
Pattern Search Optimization (PS)	0.5000	0.9142	4.5328	8.5000	3.3186	212
Gradient-based Optimization (GBO)	0.5017	0.9187	4.5220	8.4973	3.3203	26

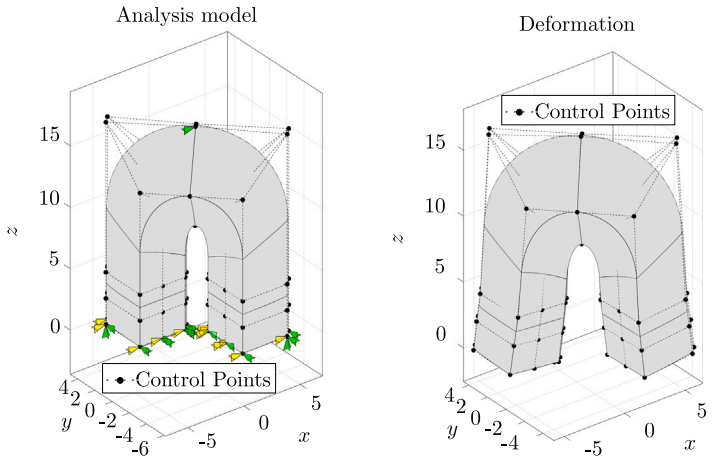

(a) Resultant geometry. (b) Horseshoe deformed shape.

Fig. 10. Resultant geometry for the lower bound results for the 3D horseshoe. Dimensions in cm.

geometry, defined by a high value of L and H, and a smaller value of R and r. Fig. 10.b shows the deformed shape due to the equal and opposite in-plane flat-edge unitary displacements. Note how the horseshoe tends to deflect its ends outward.

Fig. 11 illustrates the stress triaxiality distribution for the geometry corresponding to the lower bound of the response. Specifically, Figs. 11.a and 11.b depict the stress triaxiality in the xy−plane, while Figs. 11.c and 11.d show the stress triaxiality in the xz−plane. In particular, Figs. 11.b and 11.d highlight the stress triaxiality distribution in the deformed configuration. To understand these triaxial stress results, Fig. 12 shows the hydrostatic and von Mises stresses on the deformed horseshoe in the xy and xz planes. The highest concentration of hydrostatic stress is observed in the inner upper region of the horseshoe shape (see

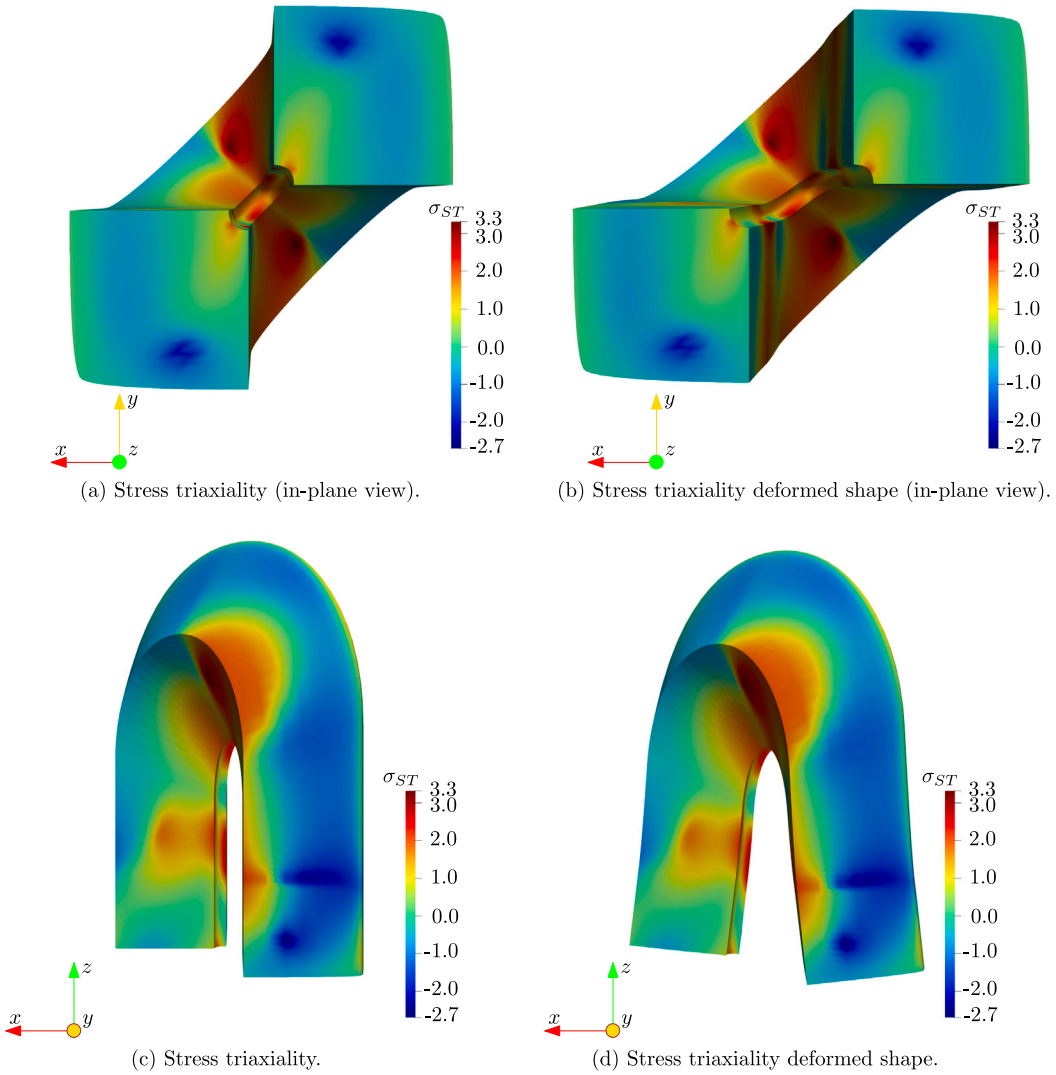

(a) Stress triaxiality (in-plane view).

(b) Stress triaxiality deformed shape (in-plane view).

(c) Stress triaxiality.

(d) Stress triaxiality deformed shape.

Fig. 11. Stress triaxiality for the lower bound results for the 3D horseshoe.

Fig. 12), leading to an increased stress triaxiality (3.3) in this region (as shown in Fig. 11). Zones of significant deformation coincide with regions of high stress, indicating potential brittle failure since increased stress triaxiality typically favors brittle fracture over ductile behavior. As shown in Fig. 8, this stress distribution is expected due to the application of opposing in-plane flat-edge unitary displacements. The calculated stress values, including both hydrostatic and von Mises stresses (see Fig. 12), are consistent with results reported in the literature [28,65].

The results for the upper bound of the maximum stress triaxiality of the solid horseshoe are shown in Table 4. The optimal value of the geometric parameters (R, r, L, H) is also shown for each optimization method used, along with the number of deterministic analyses performed. The Vertex Method requires the least number of iterations (16). However, it underestimates the upper bound of the stress triaxiality as well as the case for the lower bound. The same optimum value for the maximum stress triaxiality is achieved by all optimization algorithms considered. Nevertheless, PSO requires significantly more computations (4665), making it less efficient, than for example, SO and PS. The Gradient-based Optimization method, which requires only 20 analyses, offers the best trade-off between accuracy and computational complexity, showing the benefit of using the sensitivities from the variational approach.

Similar to the lower bound, Fig. 13.a shows the resulting geometry for the horseshoe system with the optimal values of the uncertain geometric parameters for the upper bound of the response. As expected, the upper bound of the maximum stress triaxiality

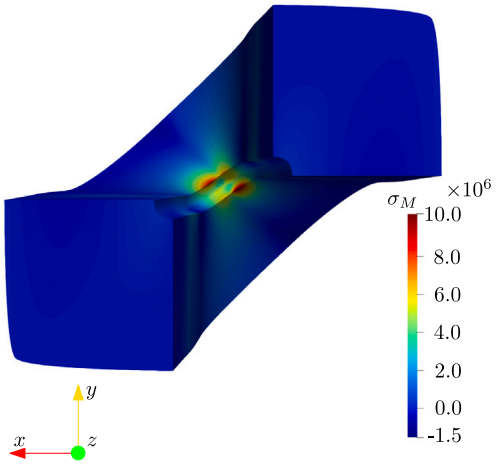

(a) Hydrostatic stress deformed shape (in-plane view).

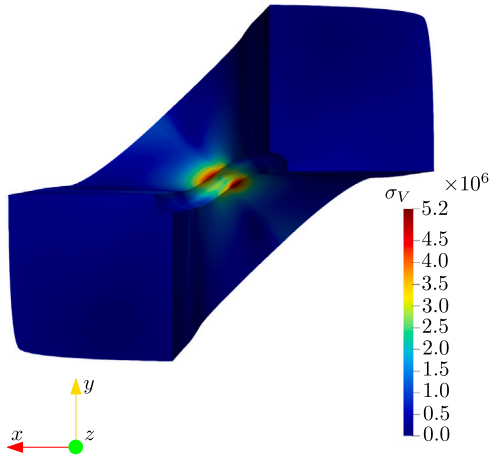

(b) von Mises stress deformed shape (in-plane view).

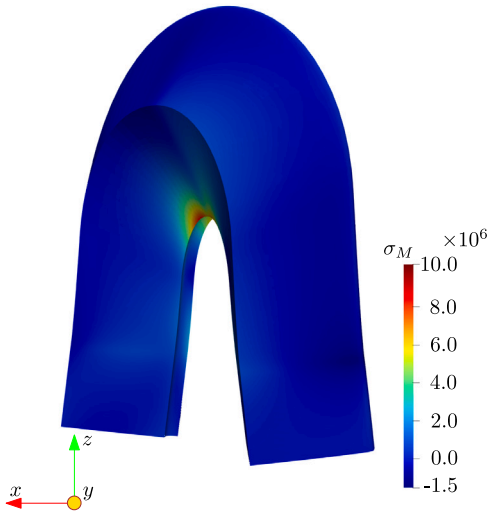

(c) Hydrostatic stress deformed shape.

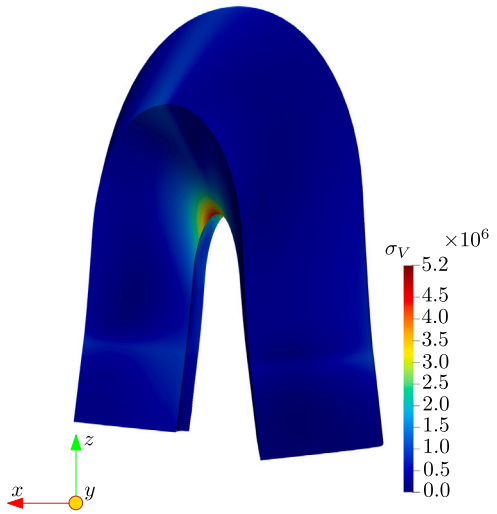

(d) von Mises stress deformed shape.

Fig. 12. Stresses for the lower bound results for the 3D horseshoe, in consistent units in Example 2.

Table 4
Results of optimization – upper bound of maximum stress triaxiality – Horseshoe 3D.

Method	R in cm	r in cm	L in cm	H in cm	max(σ_{ST})	No. Analysis
Vertex Method (VM)	1.5000	0.9142	3.5000	8.5000	4.9551	16
Particle Swarm Optimization (PSO)	1.5000	1.7979	3.6653	7.5000	5.0209	4665
Surrogate Optimization (SO)	1.5000	1.7991	3.6662	7.5000	5.0209	200
Pattern Search Optimization (PS)	1.5000	1.7979	3.6652	7.5000	5.0209	651
Gradient-based Optimization (GBO)	1.5000	1.7978	3.6652	7.5000	5.0209	20

is associated with a thin section geometry defined by a low value of L and H, a higher value of R, and more separation between the two ends of the horseshoe, i.e., a high value of r. Fig. 13.b shows the deformed shape due to the equal and opposite in-plane flat-edge unitary displacements.

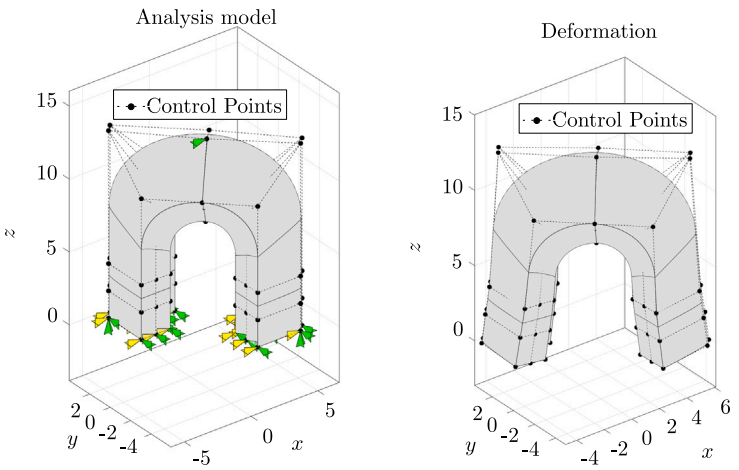

(a) Resultant geometry. (b) Horseshoe deformed shape.

Fig. 13. Resultant geometry for the upper bound results for the 3D horseshoe. Dimensions in cm.

On the other hand, Fig. 14 shows the stress triaxiality distribution within the horseshoe shape resulting from the imposed unitary displacements for the geometry resulting from the upper bound. Comparing these results with those from the lower bound geometry (see Fig. 11) shows how geometric changes affect the stress distribution. Nevertheless, the regions of high-stress concentration remain consistent in the same areas of the horseshoe. For the upper bound geometry, the stress triaxiality has a more homogeneous pattern, but with a wider range of values. In addition, the regions of high-stress triaxiality (5) are more concentrated compared to those observed in the lower-bound scenario. The elevated stress triaxiality values shown in Fig. 14 indicate critical areas that are susceptible to failure. As before, these critical areas are located where significant deformation occurs. To gain a comprehensive understanding of the stress triaxiality distribution, Fig. 15 illustrates the hydrostatic and von Mises stresses in the deformed shape. A significant concentration of both stress types is observed in the inner portion of the horseshoe, with the highest values occurring in the upper inner area.

In optimization procedures involving geometric parameters, ensuring the regularity of the stiffness matrix is essential to guarantee numerical stability and physical validity. In the examples studied, the determinant of the local deformation gradient was consistently positive, indicating the presence of physically valid configurations without element inversion. As anticipated for linear elasticity with suitable boundary conditions, the stiffness matrix remained nonsingular in these cases. Nevertheless, a significant deviation of the control points from their nominal positions could result in a negative determinant, leading to unphysical behavior, as this implies a negative mass density. Consequently, additional measures could be incorporated into the optimization process to overcome this potential problem. For example, constraints could be applied to maintain a minimum distance between certain control points to avoid self-penetration of the mesh. While these precautions are not necessary in the examples studied, they could prove valuable for complex geometries or extreme deformations.

7. Summary and conclusions

This paper explores the application of isogeometric analysis (IGA) with interval analysis for efficient quantification of the effects of geometric uncertainties on the performance of mechanical systems. The study focused on estimating the bounds of maximum stress triaxiality in a 2D hook system with uncertain radius and thickness parameters, and a solid 3D horseshoe shape with four uncertain geometric parameters.

According to the results, the implemented method, which utilizes the gradient-based optimization (GBO) approach to estimate the bounds of the response, significantly reduces the computational cost associated with uncertainty quantification in an interval context. The efficiency of the method is due to the ability of the IGA model to directly manipulate geometry and compute sensitivities without the need for costly remeshing. This benefit is achieved due to the application of a variational sensitivity analysis that allows one to compute the change of the response function concerning alterations in the uncertain parameters along with the calculation of the response of interest. To enhance the potential of IGA for uncertainty quantification within finite element users, a parametric description of the control point matrix is proposed. This approach allows the direct translation of geometric uncertainties into the

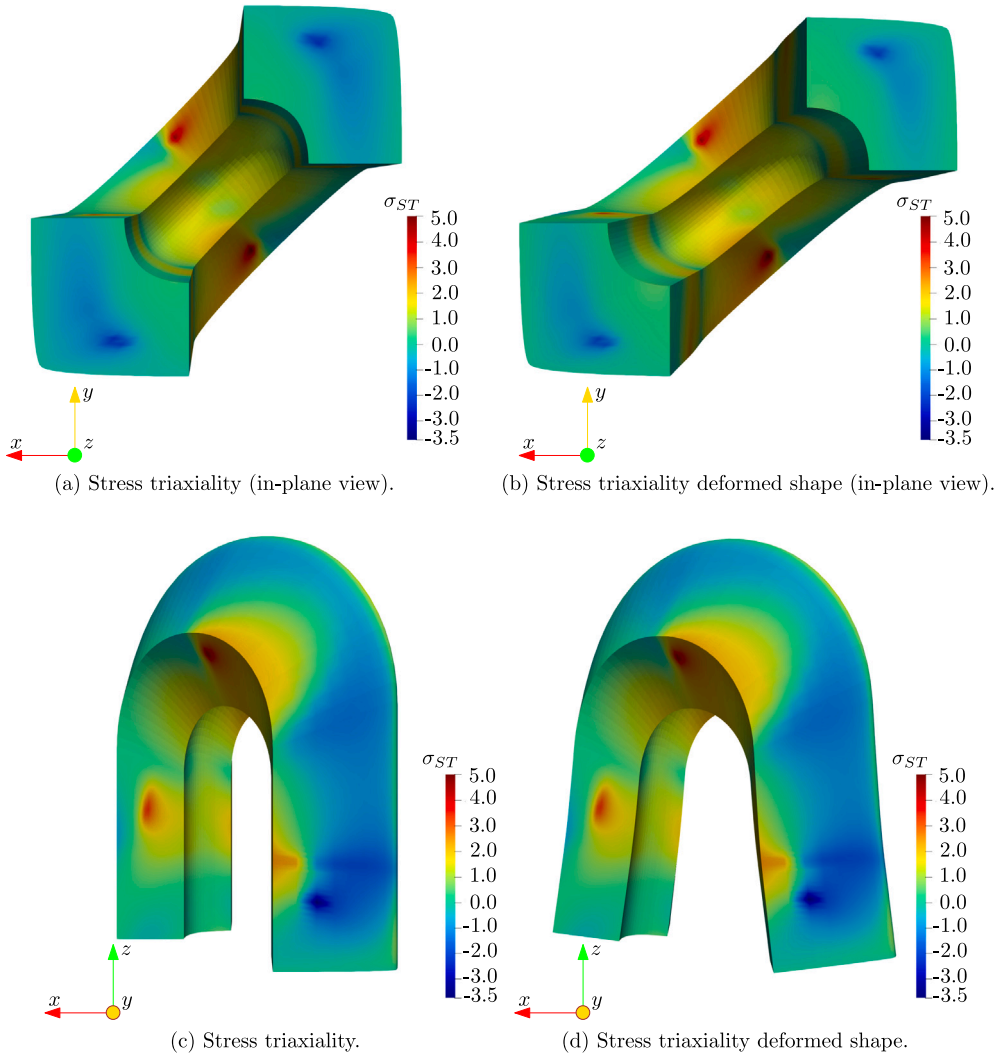

(a) Stress triaxiality (in-plane view).

(b) Stress triaxiality deformed shape (in-plane view).

(c) Stress triaxiality.

(d) Stress triaxiality deformed shape.

Fig. 14. Stress triaxiality for the upper bound results for the 3D horseshoe.

NURBS used for system representation. By incorporating uncertainty directly into the NURBS framework, this method facilitates the integration of IGA into traditional FEA workflows for geometric variation in mechanical systems.

Future work will explore the application of this method to more complex systems requiring multiple patches for their construction, and investigate its potential for other types of uncertainty description techniques, such as interval fields. In this case, the advantages of describing and propagating uncertainty using NURBS-based interval fields will be investigated. Moreover, while the present study is concerned with cases involving a limited number of uncertain parameters, extending the framework to encompass high-dimensional uncertainties, such as surface geometric uncertainties would be a logical subsequent step. Since interval fields reduce the uncertainty to that contained at the control point positions, the key to dealing with high-dimensional geometric uncertainty will be to strategically determine which NURBS control points should be treated as uncertain and which should be used solely to manipulate the geometry. Therefore, the methodology will be further examined for coupling with mesh refinement in IGA for complex geometries.

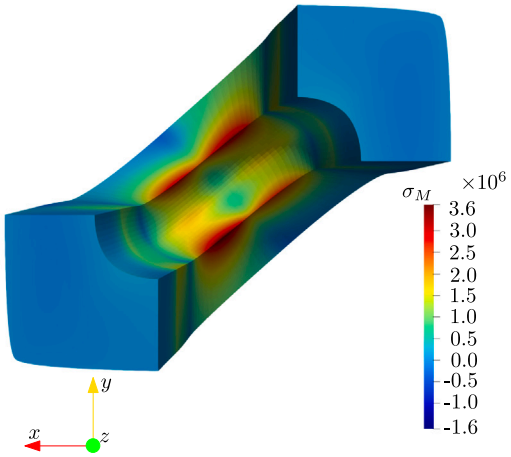

(a) Hydrostatic stress deformed shape (in-plane view).

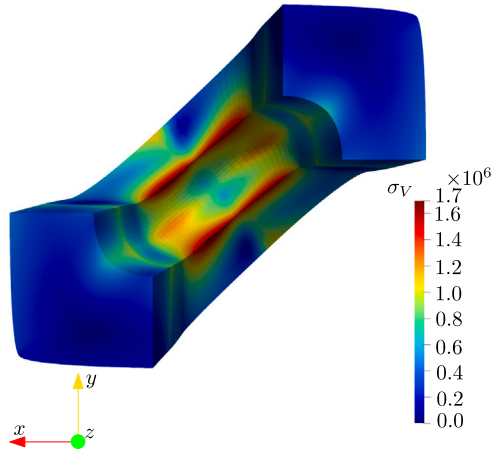

(b) von Mises stress deformed shape (in-plane view).

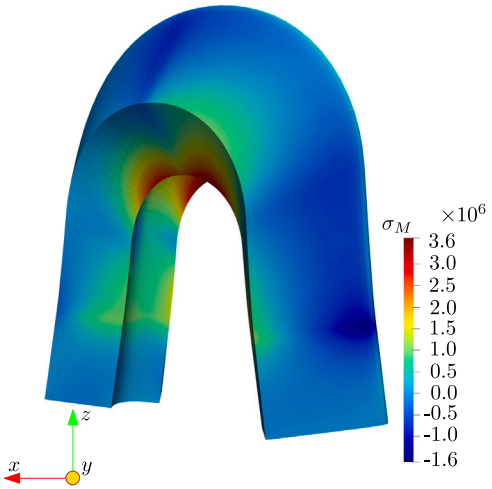

(c) Hydrostatic stress deformed shape.

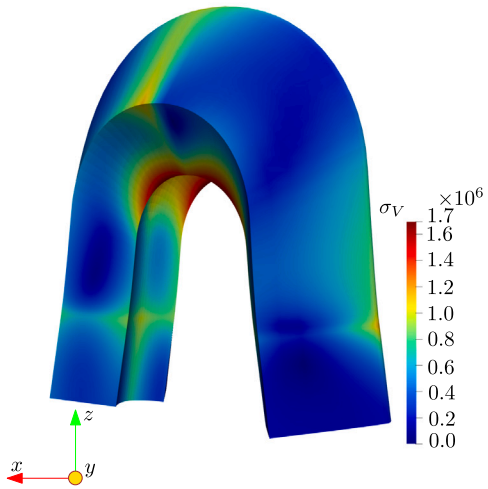

(d) von Mises stress deformed shape.

Fig. 15. Stresses for the lower bound results for the 3D horseshoe, in consistent units in Example 2.

CRediT authorship contribution statement

Nataly A. Manque: Writing – original draft, Software, Methodology, Formal analysis, Conceptualization. **Jan Liedmann:** Writing – original draft, Software, Methodology, Conceptualization. **Franz-Joseph Barthold:** Writing – review & editing, Validation, Supervision, Conceptualization. **Marcos A. Valdebenito:** Writing – review & editing, Validation, Supervision, Methodology, Conceptualization. **Matthias G.R. Faes:** Writing – review & editing, Validation, Supervision, Methodology, Conceptualization.

Declaration of competing interest

The authors declare that they have no known competing financial interests or personal relationships that could have appeared to influence the work reported in this paper.

Acknowledgment

Financial support by the Deutsche Forschungsgemeinschaft (DFG, German Research Foundation) – Project-ID 278868966 – TRR188 is gratefully acknowledged.

Data availability

Data will be made available on request.

References

[1] J. Kim, I. Lee, Modeling of geometric uncertainties in topology optimization via the shift of design nodes, Struct. Multidiscip. Optim. 65 (7) (2022) http://dx.doi.org/10.1007/s00158-022-03277-y.

[2] J. Wang, B. Wang, H. Yang, Z. Sun, K. Zhou, X. Zheng, Compressor geometric uncertainty quantification under conditions from near choke to near stall, Chin. J. Aeronaut. 36 (3) (2023) 16–29, http://dx.doi.org/10.1016/j.cja.2022.10.012.

[3] W. Chu, T. Ji, X. Chen, B. Luo, Mechanism analysis and uncertainty quantification of blade thickness deviation on rotor performance, Proc. Inst. Mech. Eng. A J. Power Energy (2023) 095765092311621, http://dx.doi.org/10.1177/09576509231162143.

[4] H. Zhang, J. Guilleminot, L.J. Gomez, Stochastic modeling of geometrical uncertainties on complex domains, with application to additive manufacturing and brain interface geometries, Comput. Methods Appl. Mech. Engrg. 385 (2021) 114014, http://dx.doi.org/10.1016/j.cma.2021.114014.

[5] H. Cheng, Z. Li, P. Duan, X. Lu, S. Zhao, Y. Zhang, Robust optimization and uncertainty quantification of a micro axial compressor for unmanned aerial vehicles, Appl. Energy 352 (2023) 121972, http://dx.doi.org/10.1016/j.apenergy.2023.121972.

[6] G. Kim, S.M. Yang, D.M. Kim, S. Kim, J.G. Choi, M. Ku, S. Lim, H.W. Park, Bayesian-based uncertainty-aware tool-wear prediction model in end-milling process of titanium alloy, Appl. Soft Comput. 148 (2023) 110922, http://dx.doi.org/10.1016/j.asoc.2023.110922.

[7] T. Cheng, S. Xiang, H. Zhang, J. Yang, New machining test for identifying geometric and thermal errors of rotary axes for five-axis machine tools, Measurement 223 (2023) 113748, http://dx.doi.org/10.1016/j.measurement.2023.113748.

[8] Y. Altintas, A. Verl, C. Brecher, L. Uriarte, G. Pritschow, Machine tool feed drives, CIRP Ann 60 (2) (2011) 779–796, http://dx.doi.org/10.1016/j.cirp.2011.05.010.

[9] J. Liu, A.T. Gaynor, S. Chen, Z. Kang, K. Suresh, A. Takezawa, L. Li, J. Kato, J. Tang, C.C.L. Wang, L. Cheng, X. Liang, A.C. To, Current and future trends in topology optimization for additive manufacturing, Struct. Multidiscip. Optim. 57 (6) (2018) 2457–2483, http://dx.doi.org/10.1007/s00158-018-1994-3.

[10] N. Nie, L. Su, G. Deng, H. Li, H. Yu, A.K. Tieu, A review on plastic deformation induced surface/interface roughening of sheet metallic materials, J. Mater. Res. Technol. 15 (2021) 6574–6607, http://dx.doi.org/10.1016/j.jmrt.2021.11.087.

[11] X. Zhang, W. Yang, M. Li, An Uncertainty Approach for Fixture Layout Optimization using Monte Carlo Method, Springer Berlin Heidelberg, 2010, pp. 10–21, http://dx.doi.org/10.1007/978-3-642-16587-0_2.

[12] F.N. Schietzold, A. Schmidt, M.M. Dannert, A. Fau, R.M.N. Fleury, W. Graf, M. Kaliske, C. Könke, T. Lahmer, U. Nackenhorst, Development of fuzzy probability based random fields for the numerical structural design, GAMM-Mitteilungen 42 (1) (2019) e201900004, http://dx.doi.org/10.1002/gamm.201900004.

[13] M. Faes, M. Broggi, E. Patelli, Y. Govers, J. Mottershead, M. Beer, D. Moens, A multivariate interval approach for inverse uncertainty quantification with limited experimental data, Mech. Syst. Signal Process. 118 (2019) 534–548, http://dx.doi.org/10.1016/j.ymssp.2018.08.050.

[14] B. Möller, M. Beer, Fuzzy Randomness, Springer Berlin Heidelberg, 2004, http://dx.doi.org/10.1007/978-3-662-07358-2.

[15] D. Zhang, L. Shu, S. Li, Fuzzy structural element method for solving fuzzy dual medium seepage model in reservoir, Soft Comput. 24 (21) (2020) 16097–16110, http://dx.doi.org/10.1007/s00500-020-04926-4.

[16] M.G. Faes, M. Daub, S. Marelli, E. Patelli, M. Beer, Engineering analysis with probability boxes: A review on computational methods, Struct. Saf. 93 (2021) 102092, http://dx.doi.org/10.1016/j.strusafe.2021.102092.

[17] M.G. Faes, M. Broggi, G. Chen, K.-K. Phoon, M. Beer, Distribution-free p-box processes based on translation theory: Definition and simulation, Probab. Eng. Mech. 69 (2022) 103287, http://dx.doi.org/10.1016/j.probengmech.2022.103287.

[18] D. Degrauwe, G. Lombaert, G.D. Roeck, Improving interval analysis in finite element calculations by means of affine arithmetic, Comput. Struct. 88 (3–4) (2010) 247–254, http://dx.doi.org/10.1016/j.compstruc.2009.11.003.

[19] A. Sofi, E. Romeo, A novel interval finite element method based on the improved interval analysis, Comput. Methods Appl. Mech. Engrg. 311 (2016) 671–697, http://dx.doi.org/10.1016/j.cma.2016.09.009, URL http://www.sciencedirect.com/science/article/pii/S004578251631129X.

[20] R.R. Callens, M.G. Faes, D. Moens, Multilevel Quasi-Monte Carlo for intercval analysis, Int. J. Uncertain. Quantif. 12 (4) (2022) 1–19, http://dx.doi.org/10.1615/int.j.uncertaintyquantification.2022039245.

[21] C. Dang, P. Wei, M.G. Faes, M.A. Valdebenito, M. Beer, Interval uncertainty propagation by a parallel Bayesian global optimization method, Appl. Math. Model. 108 (2022) 220–235, http://dx.doi.org/10.1016/j.apm.2022.03.031.

[22] V. Kreinovich, A. Lakeyev, J. Rohn, P. Kahl, Computational Complexity and Feasibility of Data Processing and Interval Computations, Springer US, 1998, http://dx.doi.org/10.1007/978-1-4757-2793-7.

[23] M. Beer, Y. Zhang, S.T. Quek, K.K. Phoon, Reliability analysis with scarce information: Comparing alternative approaches in a geotechnical engineering context, Struct. Saf. 41 (2013) 1–10, http://dx.doi.org/10.1016/j.strusafe.2012.10.003.

[24] R.E. Moore, Methods and Applications of Interval Analysis, Society for Industrial and Applied Mathematics, 1979, http://dx.doi.org/10.1137/1.9781611970906.

[25] A. Sofi, E. Romeo, O. Barrera, A. Cocks, An interval finite element method for the analysis of structures with spatially varying uncertainties, Adv. Eng. Softw. 128 (2019) 1–19, http://dx.doi.org/10.1016/j.advengsoft.2018.11.001.

[26] M. Faes, D. Moens, Recent trends in the modeling and quantification of non-probabilistic uncertainty, Arch. Comput. Methods Eng. 27 (3) (2019) 633–671, http://dx.doi.org/10.1007/s11831-019-09327-x.

[27] D. Moens, D. Vandepitte, Interval sensitivity theory and its application to frequency response envelope analysis of uncertain structures, Comput. Methods Appl. Mech. Engrg. 196 (21) (2007) 2486–2496, http://dx.doi.org/10.1016/j.cma.2007.01.006, URL https://www.sciencedirect.com/science/article/pii/S0045782507000187.

[28] T. Hughes, J. Cottrell, Y. Bazilevs, Isogeometric analysis: Cad, finite elements, nurbs, exact geometry and mesh refinement, Comput. Methods Appl. Mech. Engrg. 194 (39–41) (2005) 4135–4195, http://dx.doi.org/10.1016/j.cma.2004.10.008.

[29] J.A. Cottrell, Isogeometric Analysis, Wiley, Chichester, West Sussex, U.K, 2009.

[30] V. Agrawal, S.S. Gautam, Iga: A simplified introduction and implementation details for finite element users, J. Inst. Eng. (India): Ser. C 100 (3) (2018) 561–585, http://dx.doi.org/10.1007/s40032-018-0462-6.

[31] W. Wang, G. Chen, D. Yang, Z. Kang, Stochastic isogeometric analysis method for plate structures with random uncertainty, Comput. Aided Geom. Design 74 (2019) 101772, http://dx.doi.org/10.1016/j.cagd.2019.101772.

[32] E. Wobbes, Y. Bazilevs, T. Kuraishi, Y. Otoguro, K. Takizawa, T.E. Tezduyar, Complex-geometry iga mesh generation: application to structural vibrations, Comput. Mech. 74 (2) (2024) 247–261, http://dx.doi.org/10.1007/s00466-023-02432-6.

[33] T.D. Hien, H.-C. Noh, Stochastic isogeometric analysis of free vibration of functionally graded plates considering material randomness, Comput. Methods Appl. Mech. Engrg. 318 (2017) 845–863, http://dx.doi.org/10.1016/j.cma.2017.02.007.

[34] K. Li, W. Gao, D. Wu, C. Song, T. Chen, Spectral stochastic isogeometric analysis of linear elasticity, Comput. Methods Appl. Mech. Engrg. 332 (2018) 157–190, http://dx.doi.org/10.1016/j.cma.2017.12.012.
[35] P. Hao, H. Tang, Y. Wang, T. Wu, S. Feng, B. Wang, Stochastic isogeometric buckling analysis of composite shell considering multiple uncertainties, Reliab. Eng. Syst. Saf. 230 (2023) 108912, http://dx.doi.org/10.1016/j.ress.2022.108912.
[36] X. Lin, W. Zheng, F. Zhang, H. Chen, Uncertainty quantification and robust shape optimization of acoustic structures based on iga bem and polynomial chaos expansion, Eng. Anal. Bound. Elem. 165 (2024) 105770, http://dx.doi.org/10.1016/j.enganabound.2024.105770.
[37] H. Zhang, T. Shibutani, Development of stochastic isogeometric analysis (siga) method for uncertainty in shape, Internat. J. Numer. Methods Engrg. 118 (1) (2018) 18–37, http://dx.doi.org/10.1002/nme.6008.
[38] X. Zhang, J. Gao, L. Gao, M. Xiao, B-ito: A matlab toolbox for isogeometric topology optimization with Bézier extraction of nurbs, Adv. Eng. Softw. 191 (2024) 103620, http://dx.doi.org/10.1016/j.advengsoft.2024.103620.
[39] V.P. Nguyen, C. Anitescu, S.P. Bordas, T. Rabczuk, Isogeometric analysis: An overview and computer implementation aspects, Math. Comput. Simulation 117 (2015) 89–116, http://dx.doi.org/10.1016/j.matcom.2015.05.008.
[40] N. Antonelli, R. Aristio, A. Gorgi, R. Zorrilla, R. Rossi, G. Scovazzi, R. Wüchner, The shifted boundary method in isogeometric analysis, Comput. Methods Appl. Mech. Engrg. 430 (2024) 117228, http://dx.doi.org/10.1016/j.cma.2024.117228.
[41] J.A. Snyman, D.N. Wilke, Practical Mathematical Optimization, Springer International Publishing, 2018, http://dx.doi.org/10.1007/978-3-319-77586-9.
[42] J. Liedmann, F.-J. Barthold, Variational sensitivity analysis of elastoplastic structures applied to optimal shape of specimens, Struct. Multidiscip. Optim. 61 (6) (2020) 2237–2251, http://dx.doi.org/10.1007/s00158-020-02492-9.
[43] O.C. Zienkiewicz, The Finite Element Method, Butterworth-Heinemann, 2000.
[44] K.W. Morton, D.F. Mayers, Numerical Solution of Partial Differential Equations: An Introduction, Cambridge University Press, 2005.
[45] K.-J. Bathe, Finite Element Procedures, Klaus-Jürgen Bathe, 2014.
[46] A. Tekkaya, P.-O. Bouchard, S. Bruschi, C. Tasan, Damage in metal forming, CIRP Ann 69 (2) (2020) 600–623, http://dx.doi.org/10.1016/j.cirp.2020.05.005.
[47] M. Böddecker, M. Faes, A. Menzel, M. Valdebenito, Effect of uncertainty of material parameters on stress triaxiality and lode angle in finite elasto-plasticity—a variance-based global sensitivity analysis, Adv. Ind. Manuf. Eng. 7 (2023) 100128, http://dx.doi.org/10.1016/j.aime.2023.100128.
[48] Y. Bao, T. Wierzbicki, On fracture locus in the equivalent strain and stress triaxiality space, Int. J. Mech. Sci. 46 (1) (2004) 81–98, http://dx.doi.org/10.1016/j.ijmecsci.2004.02.006.
[49] D. Moens, M. Hanss, Non-probabilistic finite element analysis for parametric uncertainty treatment in applied mechanics: Recent advances, Finite Elem. Anal. Des. 47 (1) (2011) 4–16, http://dx.doi.org/10.1016/j.finel.2010.07.010.
[50] T. Haag, J. Herrmann, M. Hanss, Identification procedure for epistemic uncertainties using inverse fuzzy arithmetic, Mech. Syst. Signal Process. 24 (7) (2010) 2021–2034, http://dx.doi.org/10.1016/j.ymssp.2010.05.010.
[51] M. Hanss, S. Turrin, A fuzzy-based approach to comprehensive modeling and analysis of systems with epistemic uncertainties, Struct. Saf. 32 (6) (2010) 433–441, http://dx.doi.org/10.1016/j.strusafe.2010.06.003.
[52] W. Dong, H.C. Shah, Vertex method for computing functions of fuzzy variables, Fuzzy Sets and Systems 24 (1) (1987) 65–78, http://dx.doi.org/10.1016/0165-0114(87)90114-x.
[53] S.S. Rao, L. Berke, Analysis of uncertain structural systems using interval analysis, AIAA J. 35 (4) (1997) 727–735, http://dx.doi.org/10.2514/2.164.
[54] L. Catallo, Genetic anti-optimization for reliability structural assessment of precast concrete structures, Comput. Struct. 82 (13–14) (2004) 1053–1065, http://dx.doi.org/10.1016/j.compstruc.2004.03.018.
[55] A. Klimke, R. Nunes, B. Wohlmuth, Fuzzy arithmetic based on dimension-adaptive sparse grids: A case study of a large-scale finite element model under uncertain parameters, Internat. J. Uncertain. Fuzziness Knowledge-Based Systems 14 (05) (2006) 561–577, http://dx.doi.org/10.1142/s0218488506004199.
[56] Z. Deng, Z. Guo, X. Zhang, Interval model updating using perturbation method and radial basis function neural networks, Mech. Syst. Signal Process. 84 (2017) 699–716, http://dx.doi.org/10.1016/j.ymssp.2016.09.001.
[57] F.-J. Barthold, N. Gerzen, W. Kijanski, D. Materna, Efficient Variational Design Sensitivity Analysis, in: Computational Methods in Applied Sciences, vol. 40, Springer International Publishing, Switzerland, 2016, http://dx.doi.org/10.1007/978-3-319-23564-6_14.
[58] F.-J. Barthold, A short guide to variational design sensitivity analysis, in: 6th World Congress on Structural and Multidisciplinary Optimization, 2005.
[59] Penguian, Nurbs Toolbox By D.M. Spnik, MATLAB Central File Exchange, 2020, Retrieved December 14 2020. URL https://www.mathworks.com/matlabcentral/fileexchange/26390-nurbs-toolbox-by-d-m-spink.
[60] J.J. Moré, D.C. Sorensen, Computing a trust region step, SIAM J. Sci. Stat. Comput. 4 (3) (1983) 553–572, http://dx.doi.org/10.1137/0904038.
[61] R.H. Byrd, J.C. Gilbert, J. Nocedal, A trust region method based on interior point techniques for nonlinear programming, Math. Program. 89 (1) (2000) 149–185, http://dx.doi.org/10.1007/pl00011391.
[62] J. Kennedy, R. Eberhart, Particle swarm optimization, Proceedings of ICNN'95-International Conference on Neural Networks, Vol. 4, IEEE, Perth, WA, Australia, 1995, pp. 1942–1948.
[63] M.J.D. Powell, The Theory of Radial Basis Function Approximation in 1990, Oxford University Press, Oxford, 1992, pp. 105–210, http://dx.doi.org/10.1093/oso/9780198534396.003.0003.
[64] C. Audet, J.E. Dennis, Analysis of generalized pattern searches, SIAM J. Optim. 13 (3) (2002) 889–903, http://dx.doi.org/10.1137/s1052623400378742.
[65] R. Jahanbin, S. Rahman, Stochastic isogeometric analysis in linear elasticity, Comput. Methods Appl. Mech. Engrg. 364 (2020) 112928, http://dx.doi.org/10.1016/j.cma.2020.112928.